

## RADAR OBSERVATIONS OF COMET IRAS-ARAKI-ALCOCK 1983d

J. K. HARMON, D. B. CAMPBELL, AND A. A. HINE  
 National Astronomy and Ionosphere Center

AND

I. I. SHAPIRO AND B. G. MARSDEN  
 Harvard-Smithsonian Center for Astrophysics  
 Received 1987 December 8; accepted 1988 August 18

### ABSTRACT

Results and interpretation of Arecibo S-band ( $\lambda = 12.6$  cm) radar observations of comet IRAS-Araki-Alcock 1983d are presented. The observations of 1983 May 11 yield an echo with two distinct components: a strong narrow-band echo from the nucleus and an unexpected broad-band echo from large particles. The inferred diameter of the nucleus based on the strength of the narrow-band echo ranges from 5 km for a solid-ice surface to 16 km for a surface of loosely packed snow; the 10 km diameter inferred from thermal emission data would require a surface with a radar reflectivity typical of that of moderately packed snow. The nucleus surface is asteroid-like in that it appears to be very rough on scales of a few meters or more. The radar data imply a nucleus rotation period of 2–3 days. The broad-band echo is only the second deep-space particle population detected with radar. The extremely low (1%) circular depolarization measured for this component implies a maximum particle radius of a few centimeters, whereas various other considerations set a minimum effective radius of 1 cm for the echo-producing particles. A reasonably consistent model of the broad-band echo is developed on the basis of a simple gas-drag theory for particle ejection from the nucleus. The radar data indicate that the large grains are predominantly from the sunlit hemisphere but with a mean ejection direction which is offset from the solar direction; this offset agrees with the orientation of the infrared/visual dust emission fan. Most of the large grains appear to be confined to a 1000 km radius centered on the nucleus. The large grains are an order of magnitude more abundant than is expected from a simple  $a^{-4.2}$  power-law extrapolation of the dust-particle production size distribution  $n(a)$ . While this implies that the large (millimeter to centimeter size) grains account for a significant fraction of the total mass loss in particles, it does not pose any problems for the mass-loss budget of the nucleus. The implications of these results for future radar observations is discussed.

*Subject headings:* comets — radar astronomy

### I. INTRODUCTION

Few comets approach the Earth closely enough to be probed with radar. Only two comets, the periodic comets Encke and Grigg-Skjellerup, had been detected by radar prior to 1983. The echoes from these objects were consistent with reflection from solid nuclei up to a few kilometers in diameter (Kamoun *et al.* 1982; Kamoun, Pettengill, and Shapiro 1982; Kamoun 1983). In addition, bounds were placed on the spin vectors of these comets. However, little else could be inferred from these observations because of intrinsic ambiguities and the weakness of the radar echoes. In 1983 May the newly discovered comet IRAS-Araki-Alcock 1983d made the closest known approach to the Earth of any comet since 1770. The approach distance of IRAS-Araki-Alcock (IAA) was only one-tenth that of comet Encke in 1980. Given the (distance) $^{-4}$  dependence of the strength of the radar echoes, the close approach of IAA afforded the opportunity to detect very strong signals.

Radar observations of comet IAA were made at Arecibo Observatory on 1983 May 11 and at Goldstone on May 11 and 14. As expected, a very strong, concentrated echo was obtained from the comet nucleus (Campbell *et al.* 1983; Goldstein, Jurgens, and Sekanina 1984). In addition, both observatories made the unanticipated detection of a broad-band echo component which was clearly distinct from the nucleus echo and which contributed a significant fraction of the total echo power. From preliminary analyses, Shapiro *et al.* (1983) con-

cluded that a “cloud” of unexpectedly large particles ejected from the comet was the source of this echo component (see also Goldstein, Jurgens, and Sekanina 1984).

In this paper we present a detailed analysis and interpretation of the Arecibo radar echo from comet IAA. The very high signal strengths permitted accurate determination of the shape of the echo spectrum in the two orthogonal senses of circular polarization. From a study of the narrow-band component, we place constraints on the size, rotation period, reflectivity, and roughness of the nucleus. Our detailed analysis of the broad-band component yields estimates of, or bounds on, the spatial extent, position, and mass of the particle cloud, as well as the effective size of the constituent particles. Considerable literature on comet IAA has accumulated since 1983, and, hence, much of our interpretation involves comparisons of Arecibo results with other observational data; the latter include Goldstone radar observations, the radio continuum observations, and the multiband (ultraviolet, infrared, visual) imagery and spectrophotometry.

### II. OBSERVATIONS AND DATA ANALYSIS

Comet IAA was discovered a scant week before the close approach. Obtaining enough reliable optical observations to determine a useful ephemeris for radar observations during this close passage was therefore a challenging task, because of both the rapid motion of the comet across the sky and the large

number of relatively inexperienced observers involved. This task was barely accomplished in time for radar observations to be made on 1983 May 11, the one and only date on which the comet passed within view of the Arecibo Observatory's radar. In fact, two sets of ephemerides were developed, with the second, more accurate one arriving at Arecibo by telephone some 10 minutes after observations had begun.

IAA's extremely rapid motion in declination near its approach to Earth, coupled with the Arecibo telescope's restricted sky coverage, limited our radar observations to a single 2 hr 40 minute period, centered on 1983 May 11.92 (UT). At that epoch the distance to the comet was 0.033 AU, slightly greater than its 0.031 AU distance at perigee (9 hr earlier). Our observations were made in the continuous-wave (CW) mode; an unmodulated (monochromatic) wave was transmitted, and the received echo was Fourier-analyzed to yield the spectrum of the echo from the comet. An observation of this type provides no useful estimate of the distance to the target, and hence no direct indication of its size. Such ranging observations, though obviously desirable, were not feasible because of the combination of the short observing window and the large uncertainty in the predicted range.

The radar observations were made with the S-band (2380 MHz,  $\lambda = 12.6$  cm) radar on the 305 m diameter telescope at Arecibo, Puerto Rico. The transmissions were right-circular polarized with a continuous power of 370 kW; the one-way antenna gain was 71 dB. A dual-channel maser receiver provided simultaneous reception of both the right- and left-circular polarized components of the echo signal. The system noise temperature varied over the range 35–85 K.

The observations were composed of transmit/receive cycles, repeated at 2 minute intervals. Each cycle consisted of a transmit period of 31 s (the approximate round-trip light-travel time) followed immediately by a receive period of equal duration. The relatively long (2 minute) cycle time and corresponding data loss were unavoidable given the available observing system and data-taking program (which were not designed for such short round-trip times). Usable data were obtained between 21:35 and 23:25 UT from a total of 46 transmit/receive cycles. The coherently detected signal for each polarization channel was sampled continuously at a 4 kHz rate during each receive period. These (complex) samples were recorded on magnetic tape for later analysis.

To determine the spectrum of the echoes accurately, corrections had to be made for the frequency drift caused by changes with time in the radial velocity of the comet's center of mass with respect to the radar. An approximate compensation for this drift was made during the observations by continually adjusting the programmable local oscillator of the receiver system according to the comet ephemeris. The local oscillator was adjusted 200 times per second, which, given the  $6 \text{ Hz s}^{-1}$  comet motion, resulted in a quantization smear of about 0.03 Hz. This smear was negligible compared with that due to inaccuracies in the ephemerides, especially the first one. To find the errors in the corrections for this drift, we used an empirical approach. First, a low-resolution (0.977 Hz) analysis was made in which the echo center frequency was estimated for the average spectrum from each transmit/receive cycle. The ephemeris drift was found to be very nearly linear; least-squares fits gave drift rates of  $-0.06$  and  $-0.016 \text{ Hz s}^{-1}$  for the first and second sets of ephemerides, respectively. These computed rates were then used in a second, higher resolution (0.244 Hz) spectral analysis. For this second analysis we com-

pensated for frequency drifts and offsets by multiplying the time series by a complex phase factor  $\exp[i\phi(t)]$  prior to Fourier transforming. Averaging the spectra in blocks of five transmit/receive cycles and comparing their center frequencies revealed a residual nonlinear drift component with an amplitude of 0.6 Hz. The smooth form of this residual drift enabled us, through addition of a fine-correction term to the phase rotation  $\phi(t)$ , to correct for all frequency drifts and offsets to an accuracy of  $\pm 0.02$  Hz. The third and final analysis step consisted of a reanalysis of the data using the fine-corrected phase rotation and long (32 K) transforms to yield a high-resolution (0.122 Hz) spectrum in each polarization for each successive 8.2 s data block. The individual spectra were then summed to produce a weighted-average spectrum from which a linear baseline, attributed primarily to receiver noise, was removed.

The resolution of 0.122 Hz was adequate for distinguishing some of the fine structure in the echo spectrum of the nucleus without introducing excessive self-noise, that due to fluctuations in phase and amplitude of the echoes caused by slight changes in the orientation of the comet with respect to the line of sight from it to the radar. For the nucleus echo, this self-noise dominated the contribution of the radar system noise; thus the root mean square (rms) of the fluctuations in each frequency-resolution cell was equal to the mean power in that cell divided by the square root of the number  $N$  of equivalent spectra that were averaged together. To maximize  $N$ , we weighted the data to give equal echo signal amplitude prior to summing. The average spectrum for the day (see Fig. 1) was formed by summing 143 spectra (typically three spectra per transmit/receive cycle), giving a fractional statistical uncertainty of 0.08. For the broad-band skirt echo (Fig. 2) a different weighting scheme was used in order to give the best spectral estimator for the extremely weak depolarized echo. This was necessary because the depolarized skirt echo, unlike the nucleus echo, had a spectral density which was actually less than that of the system noise. Thus the optimal estimator was one which maximized the ratio of the amplitude of the depolarized skirt echo spectrum to the rms statistical fluctuations in the system noise spectrum. In this case the optimal weighting is one which weights each spectrum by the ratio of the signal (echo) power to the square of the system noise power. At Arecibo this weighting factor changes with time because of known systematic variations in antenna gain and temperature with source zenith angle. We implemented the weighting by adjusting the individual spectra to give equal system noise amplitude and then weighting by the expected signal-to-noise ratio computed from the known zenith-angle dependences.

### III. RESULTS

The radar echo of comet IAA, as mentioned, consisted of two separate components which could be distinguished clearly by their spectral shapes and polarization properties. We identify the narrow-band component with reflections from the nucleus and the broad-band component with reflections from a cloud of small objects (Campbell *et al.* 1983; Shapiro *et al.* 1983). The various spectra are shown in Figures 1 and 2, and discussed below. Characteristics of these components, estimated from the spectra, are listed in Table 1 and are also discussed below.

#### a) Narrow-Band (Nucleus) Component

The spectrum for the narrow-band component, averaged over all of the usable data for each polarization, is shown in

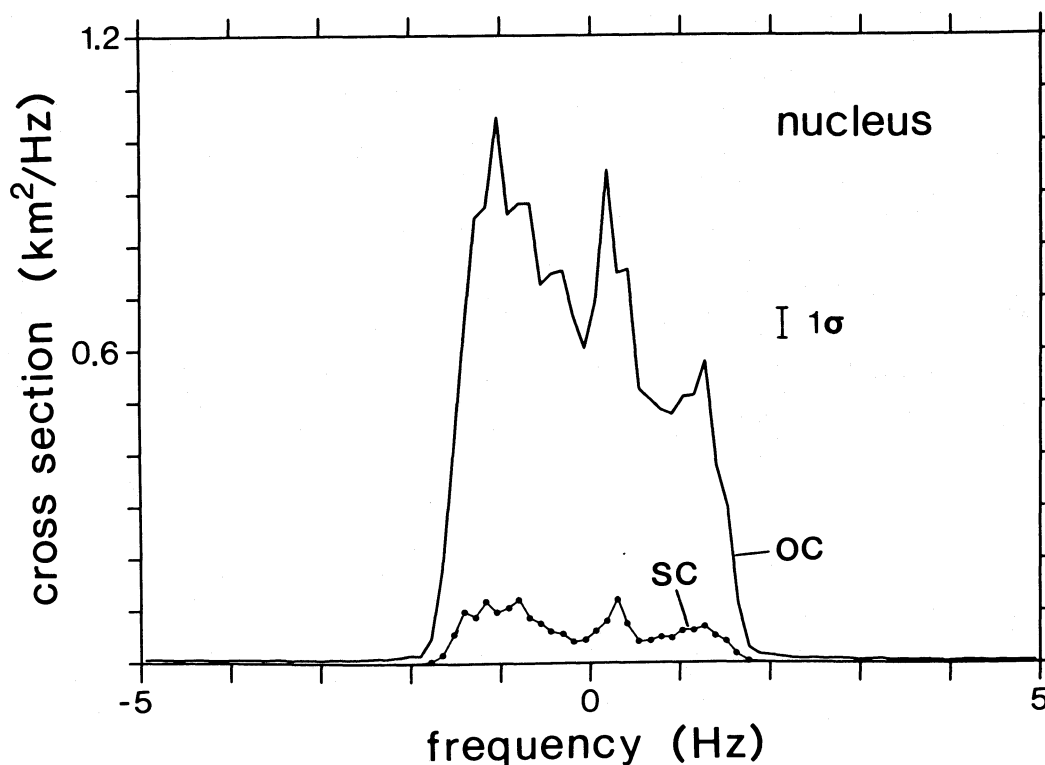


FIG. 1a

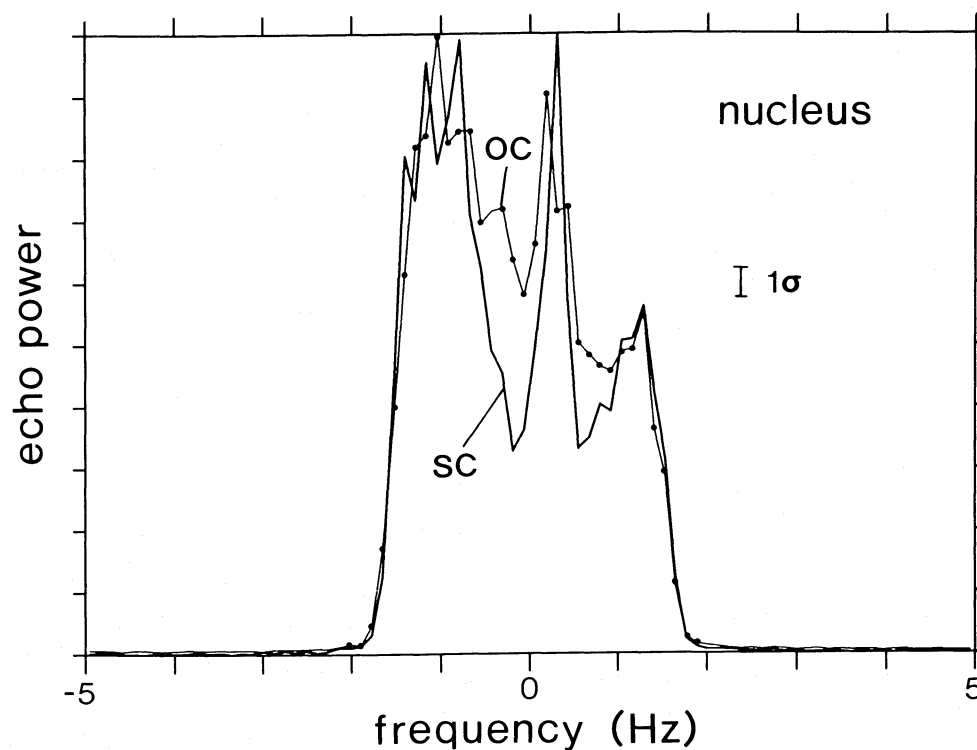


FIG. 1b

FIG. 1.—(a) Spectrum of the radar echo from the nucleus, averaged over the full observing session. The OC (“polarized”) and SC (“depolarized”) components are indicated. The error bar denotes the spectral estimation error ( $1\sigma$ ) for the top portion of the OC spectrum. The echo center frequency is 0 Hz by definition. (b) The same OC and SC spectra shown in (a), but with each normalized to its respective maximum amplitude (linear vertical scale). Note that the spectral features are more prominent in the SC than in the OC spectrum.

TABLE 1  
12.6 CENTIMETER RADAR RESULTS FOR COMET  
IRAS-ARAKI-ALCOCK

PARAMETER	COMPONENT	
	Nucleus	Particle Cloud (skirt)
$\sigma$ (km <sup>2</sup> )	$2.37 \pm 0.5$	$0.81 \pm 0.16$
$\mu_c$	$0.105 \pm 0.005$	$0.014 \pm 0.003$
$BW_f$ (Hz)	$3.5 \pm 0.1$	$600 \pm 50$
		$470 \pm 30$ (1% maximum)
$BW_h$ (Hz)	$2.9 \pm 0.1$	$72 \pm 3$

NOTE.—In the first column,  $\sigma$  is the total radar cross section (including depolarized echo) and  $\mu_c$  is the circular polarization ratio  $\sigma_{sc}/\sigma_{oc}$ .  $BW_f$  is the full bandwidth of the spectrum (equivalent to  $f_0$  for the nucleus); for the skirt we quote both the full bandwidth visible above the noise and the bandwidth at 1% of the maximum amplitude.  $BW_h$  is the spectrum bandwidth at the half-power level.

Figure 1. The amplitude, bandwidth, general shape, and polarization properties of each spectrum are consistent with expectations for echoes from a compact nucleus. The stronger echo is in the so-called polarized sense, i.e., the circular polarization sense which is orthogonal to the sense of the transmitted wave. This is the polarization in which one would expect all of the echo power in the case of a purely specular reflection. A much weaker echo is found for the “depolarized” sense, i.e., the circular polarization sense which is the same as that transmitted. A depolarized echo is usually interpreted as evidence for polarization randomization by wavelength-scale structure or multiple scattering. We will use the notation OC and SC to specify the polarized (orthogonal circular) and depolarized (same circular) senses, respectively, and the symbol  $\mu_c$  to denote the ratio of the radar cross sections,  $\sigma$ , of the target for these two modes:  $\mu_c = \sigma_{sc}/\sigma_{oc}$ .

Comet IAA is the first comet for which SC echoes have been detected; Kamoun (1983) set an upper limit for  $\mu_c$  of 0.3 at  $\lambda = 12.6$  cm for comet Grigg-Skjellerup. Our measurement of  $\mu_c = 0.105 \pm 0.005$  shows that the nucleus of IAA does not depolarize strongly at  $\lambda = 12.6$  cm. The Goldstone X-band ( $\lambda = 3.5$  cm) radar observations of 1983 May 14 (Goldstein, Jurgens, and Sekanina 1984) showed significantly stronger nucleus depolarization ( $\mu_c = 0.25$ ) at the smaller wavelength. The Goldstone S-band (12.9 cm) radar observations of IAA, made at the same time as the Arecibo observations, involved only reception in the OC polarization.

Our polarized cross section  $\sigma_{oc}$  of IAA of  $2.14 \pm 0.4$  km<sup>2</sup> is the largest yet measured for a comet nucleus (the large uncertainty is due primarily to difficulties in calibrating the Arecibo radar system accurately). For comparison, comets Encke and Grigg-Skjellerup gave cross sections of  $1.1 \pm 0.7$  and  $0.5 \pm 0.13$  km<sup>2</sup>, respectively (Kamoun *et al.* 1982; Kamoun 1983). Our  $2.14$  km<sup>2</sup> value is in agreement with the  $2.25$  km<sup>2</sup> value for  $\sigma_{oc}$  from the Goldstone S-band observations (Goldstein, Jurgens, and Sekanina 1984).

IAA is the first comet for which the spectrum was resolved and, hence, the first to have features observed in its echo spectrum. The OC and SC spectra, in fact, exhibit the same features, despite the large difference in their amplitudes. This similarity can be seen best from Figure 1b, which shows both spectra normalized to their respective maxima. The spectra have very sharp edges, an overall “skew” toward negative frequencies, and three statistically significant peaks. Note, too,

that the peaks are more prominent in the SC spectrum than in the OC spectrum.

#### b) Broad-Band (Particle Cloud) Component

To exhibit the broad-band component of the echo spectra, we show in Figure 2a the OC and SC spectra on a much expanded frequency scale with the amplitude truncated at about 2% of the OC maximum. The narrow nucleus echo (centered, by definition, at 0 Hz) is flanked by a broad-band feature whose peak is at approximately  $-30$  Hz. Extensive system tests confirmed the reality of this unexpected echo component; moreover, a similar feature was detected by the Goldstone radar (Goldstein, Jurgens, and Sekanina 1984). We will refer to this broad-band feature as the “skirt” component to be consistent with Goldstein *et al.* Our estimated cross section of the skirt is  $0.8 \pm 0.2$  km<sup>2</sup>, or about 25% of the total radar cross section of IAA. A similar cross section was reported from the 12.9 cm observations at Goldstone on May 11 (Goldstein, Jurgens, and Sekanina 1984). The dual-polarization 3.5 cm observations at Goldstone on May 13 did not yield a detectable skirt echo (R. Jurgens 1987, private communication), placing an upper bound of roughly 6 km<sup>2</sup> for its cross section at this wavelength. This result bears on our size estimates (see § Vc) of the objects giving rise to the skirt echo.

The 0.122 Hz frequency resolution used to distinguish features in the echo spectrum of the nucleus yielded an OC spectrum for the skirt which was heavily overresolved; moreover, the SC spectrum of the skirt was then barely detectable above the statistical noise fluctuations (see Fig. 2a). To estimate the shape of the skirt spectrum better, we smoothed the spectra of Figure 2a by convolving each with a 10 Hz wide rectangular window. Prior to smoothing, we removed the nucleus component by interpolating across the several hertz of spectrum containing the nucleus echo and those adjacent frequencies contaminated by leakage of nucleus power into sidelobes of the  $[\sin(\pi f)/f]^2$  spectral response function. The smoothed spectra are shown in Figure 2b. The OC spectrum is nearly symmetric about  $-30$  Hz except for a slight bulge at  $-100$  Hz. OC echo power is detectable over a bandwidth of roughly 600 Hz. In Figure 2c we compare the Arecibo OC skirt spectrum with the corresponding spectrum obtained at Goldstone (Goldstein, Jurgens, and Sekanina 1984). Despite the lower signal-to-noise ratio achieved at Goldstone, the similarity between the spectra obtained at the two facilities is clear. Both spectra have roughly the same width and negative-frequency offset.

The SC echo in Figure 2b appears similar to the OC echo, but has a much lower amplitude; we measure a  $\mu_c$  for the skirt of  $0.014 \pm 0.003$ , after correcting for polarization cross-coupling. The quoted uncertainty is dominated by that of the measurement of the polarization isolation of the antenna. These measurements, made a few days after the comet observations, indicated a “cross-coupling” of the polarizations of  $0.010 \pm 0.003$  for a radio source at the beam center. The remarkably low polarization ratio measured for the skirt echo provides a key constraint for its interpretation, as is discussed in § Va.

#### IV. NUCLEUS: INFERRED PROPERTIES

##### a) Roughness and Figure

The shape of the nucleus Doppler spectrum is determined by (1) the statistical properties of the surface roughness, (2) the degree of homogeneity of the surface scattering, and (3) the



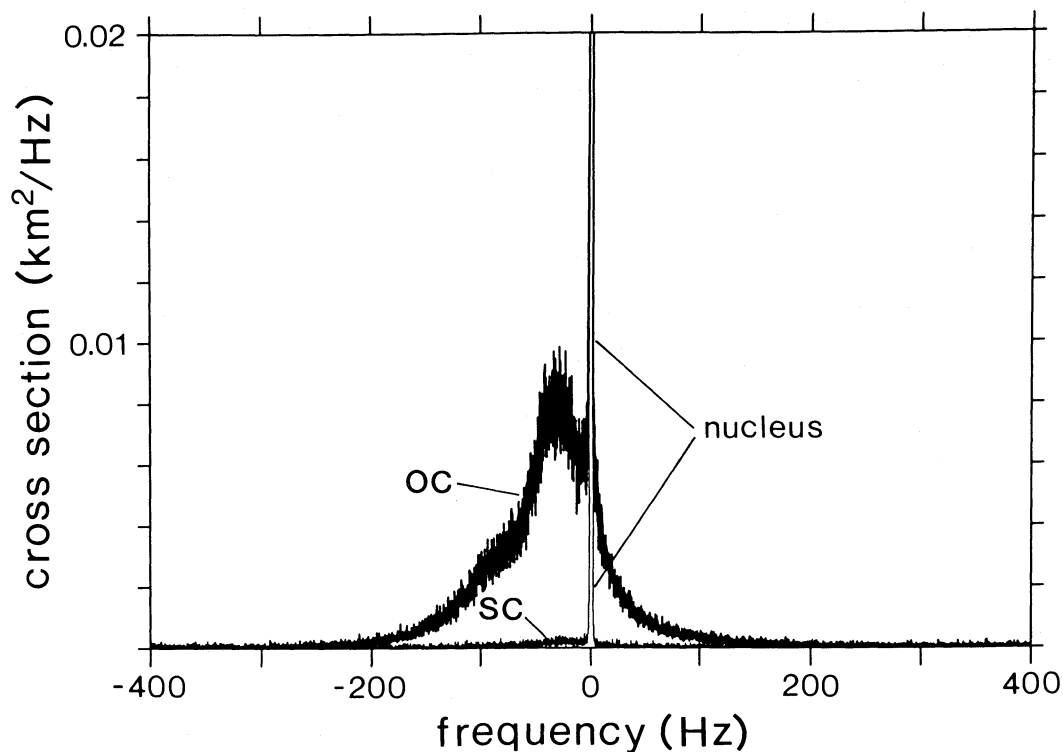


FIG. 2a

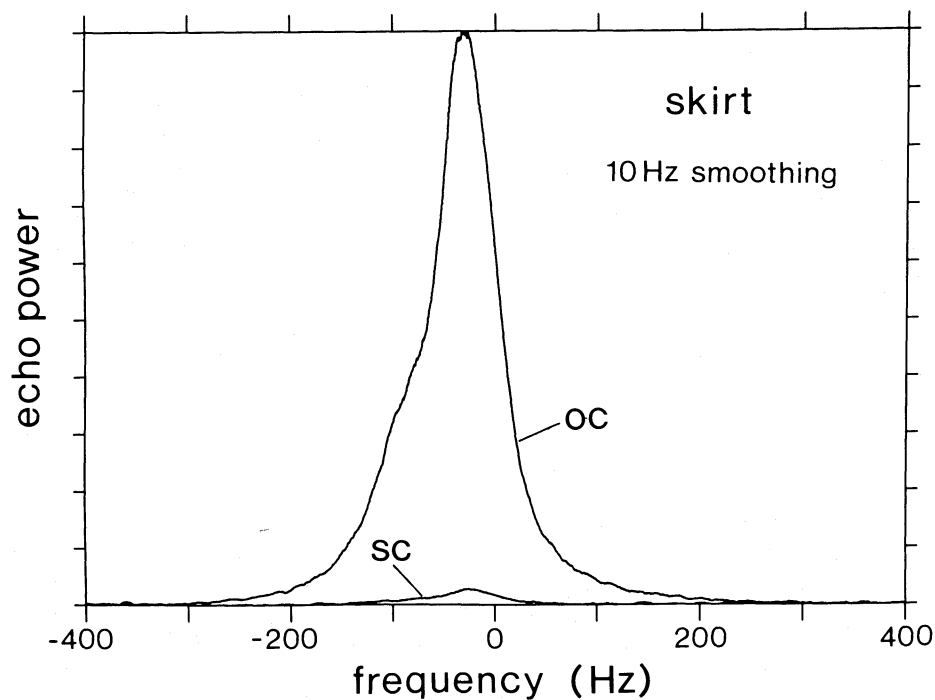


FIG. 2b

FIG. 2.—(a) OC and SC spectra truncated at 2% of the maximum OC amplitude. The narrow nucleus component can be seen flanked by the much broader skirt component. (b) Skirt spectrum of (a) after smoothing with a 10 Hz rectangular-window filter (linear vertical scale). The nucleus component was removed prior to smoothing. Note the extremely low SC relative to OC power. (c) Arecibo and Goldstone OC skirt spectra normalized to their respective maximum amplitudes (linear vertical scale). The Goldstone spectrum was copied from Fig. 5 of Goldstein, Jurgens, and Sekanina (1984). The error bar gives the approximate rms error in the Goldstone spectrum.

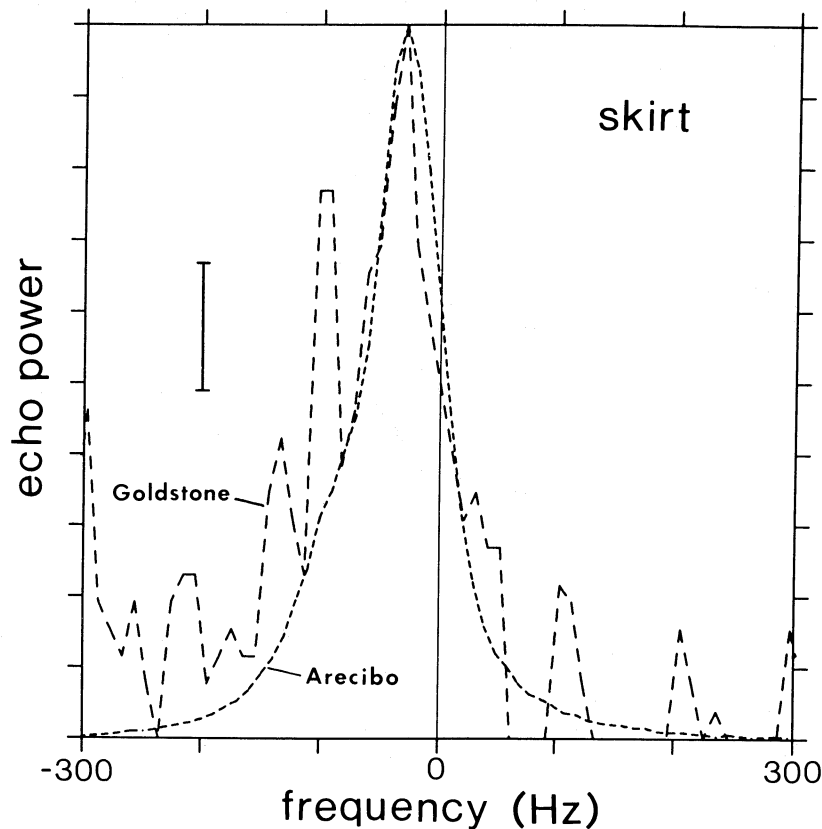


FIG. 2c

nucleus figure. The “squared-off” shape of the spectrum is indicative of an extremely rough surface which gives appreciable backscatter all the way to the limbs, where the incidence angle with the mean surface is high. Although “high-angle” backscatter is also seen in the so-called diffuse component of echoes from the Moon and terrestrial planets, the shape and polarization of the IAA nucleus echo imply a scattering surface which is quite different in character from that of these larger bodies. The most commonly applied scattering model for the diffuse scatter from rough surfaces is the cosine power law  $\sigma_0(\theta) \propto \cos^n \theta$ , where  $\sigma_0(\theta)$  is the “specific cross section” for backscatter from a surface at incidence angle  $\theta$ . For a rotating spherical target, this corresponds to a Doppler spectrum of the form  $\sigma(f) \propto [1 - (2f/f_0)^2]^{n/2}$ , where  $f_0$  is the limb-to-limb bandwidth. In Figure 3a we show this model spectrum for several values of  $n$ . The limb-darkened case  $n = 2$  (Lambert law) is generally taken to be indicative of diffractive scattering by wavelength-scale structure. On the other hand, the  $n = 1$  (uniform brightness) case is more likely to arise from scattering by larger scale structure where shadowing is important, since shadowing tends to remove from view preferentially those surfaces with surface normals inclined well away from the backscatter direction (Evans 1969; Brockelman and Hagfors 1966). Comparison of the curves in Figure 3a with the spectra in Figure 1 rules out Lambert scattering and suggests that the nucleus may be limb-brightened. This is consistent with the low depolarization ( $\mu_c = 0.10$ ) measured for the nucleus. Scattering from wavelength-scale structure would produce a somewhat higher  $\mu_c$ ; such scattering apparently dominates the diffuse components of the Moon and terrestrial planets, for which  $\mu_c$  values of 0.3–0.5 and  $n$  values of 1.5–2 are typical.

Although the comet surface must be very rough to give the observed high-angle backscatter, the scattering is clearly more specular in character than that associated with the diffuse echoes from planets. Both the polarization and spectral shape of the nucleus echo for IAA are similar to those found from S-band radar observations of several main-belt asteroids. Ostro, Campbell, and Shapiro (1985) state that most of the radar-detected main-belt asteroids appear to have very rough surfaces on scales of several meters or larger. Our results indicate that this description should hold for comet IAA as well.

The  $\mu_c$  value of 0.25 measured for the nucleus of IAA at  $\lambda = 3.5$  cm by Goldstein, Jurgens, and Sekanina (1984) indicates a strong wavelength dependence for the depolarization. This implies that there is an excess of smaller structure at X-band scales which gets “smoothed over” at S-band. One interesting possibility is that this centimeter-scale structure consists of large grains which are similar to those giving rise to the skirt echo but which, for some reason, have not been blown off the nucleus surface. Diffractive scattering from this small structure might (along with comet figure) account for the flatness of the positive-frequency tail of the X-band spectrum (see Goldstein, Jurgens, and Sekanina 1984).

Inspection of Figure 1b shows that the degree of depolarization varies across the nucleus spectrum. The deep nulls seen between the SC spectral features are largely filled in for the OC spectrum. The most likely source of this extra OC power is pure specular reflection from large facets observed at relatively small incidence angles to the mean surface. This would be analogous to the “quasi-specular component” of terrestrial planet echoes. The narrow central peak, especially prominent in the SC spectrum, is the best candidate for a feature arising

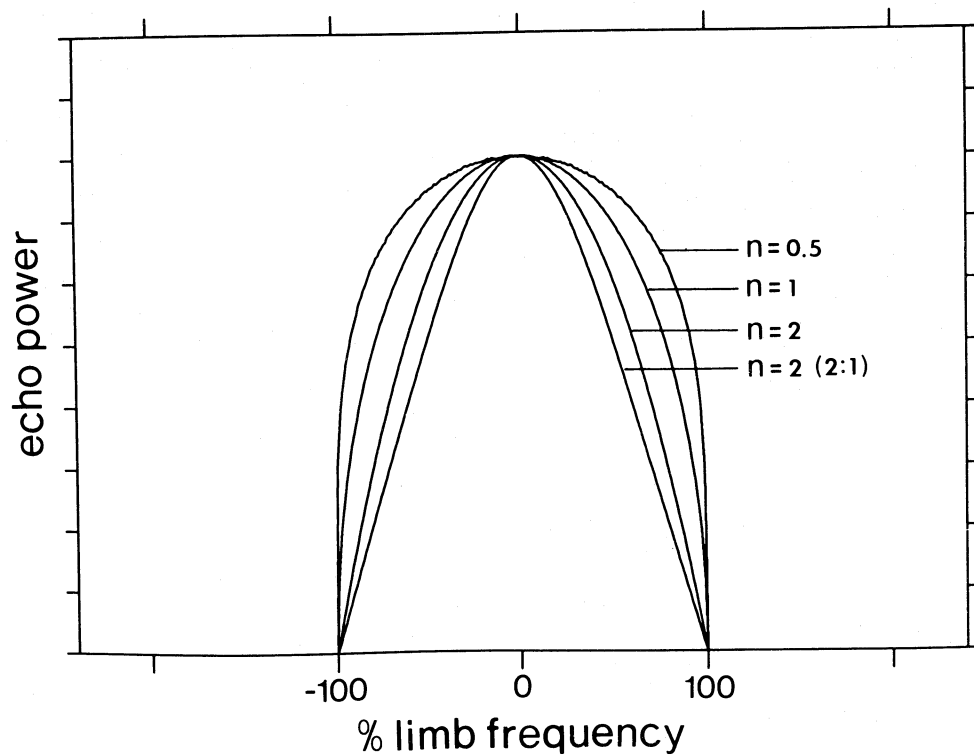


FIG. 3a

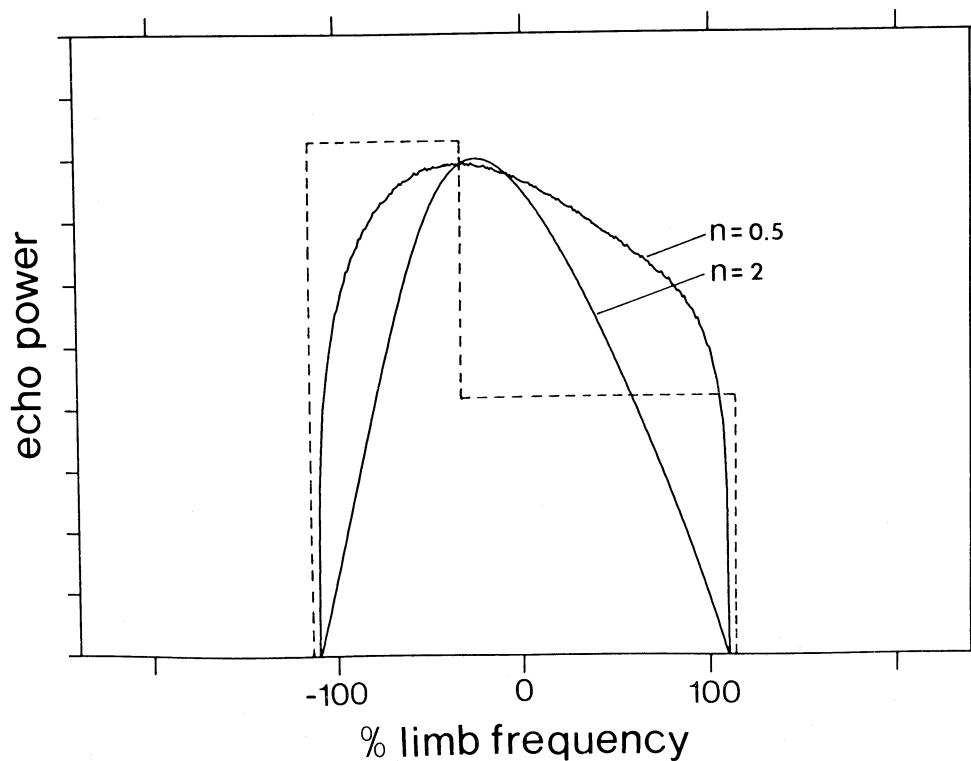


FIG. 3b

FIG. 3.—(a) Computed echo spectra for a nucleus with an assumed  $\cos^n \theta$  scattering function (linear vertical scale). Curves are shown for a spherical nucleus ( $n = 0.5, 1.0, 2.0$ ) and for a 2:1 prolate spheroid observed end-on ( $n = 2.0$ ). (b) Computed echo spectra for an aspherical nucleus rotating about a short axis normal to the line of sight and observed with its long axis inclined by  $15^\circ$  to the line of sight (linear vertical scale). Shown are the spectra for a 2:1 prolate spheroid (solid curves) with  $n = 0.5, 2.0$ , and for a 2:1:1 rectangular solid (dashed line) with  $n = 1.0$ .

from a surface scattering inhomogeneity. It is the most highly depolarized feature in the spectrum ( $\mu_c = 0.25$ ) and, thus, is unlikely to be a specular glint from the center of the disk. Such a feature could easily be explained by an outcrop of consolidated material which backscatters more efficiently than the rest of the surface. Because of the low radar reflectivity and density which we deduce for the nucleus surface overall (see next section), such a local increase in reflectivity would not be difficult to achieve.

Although the Doppler spectrum drops off sharply at both limbs, it does show a skew toward negative frequencies which would be most easily explained by a departure of the nucleus figure from sphericity. Based on an observed increase in Doppler bandwidth between May 11 and May 14, Goldstein, Jurgens, and Sekanina (1984) have modeled the nucleus of IAA as a 6:3:2 triaxial ellipsoid which rotates about its short axis and which has its long axis roughly aligned with the line of sight on May 11. If observed off-axis, such an elongated figure would give a skewed spectrum. This can be seen in Figure 3b, which shows model spectra for the case of a 2:1:1 prolate spheroid observed at a rotational phase of  $15^\circ$  with respect to the line of sight. Note that the failure of the Lambert law ( $n = 2$ ) is even more obvious than for the case of a spherical figure. This can also be seen from Figure 3a, which shows model spectra for an elongated nucleus observed end-on. In Figure 3b we also show the model spectrum for the case of a more highly faceted figure, in this case a 2:1:1 elongated rectangular solid with  $n = 1$  scattering law observed at a rotation-

al phase of  $15^\circ$ . This model gives a better approximation to the "blocky" appearance of the SC spectrum and, presumably, to that portion of the OC spectrum from which a purely specular component has been subtracted (see above).

#### b) Size, Reflectivity, and Rotation

To estimate the Fresnel reflection coefficient  $\rho_0$  of the nucleus surface we will use the approximation

$$\rho_0 \cong \sigma / (g\pi R^2), \quad (1)$$

where  $\sigma$  is the radar cross section,  $g$  is the backscatter gain, and  $R$  is the radius of the assumed spherical nucleus. Although this equation strictly holds only for specular scattering, the measured depolarization is sufficiently low to warrant using it as a first approximation (see Ostro 1985). For a homogeneous surface layer, we can obtain the dielectric constant  $\epsilon$  from,

$$\epsilon = (1 + \rho_0^{1/2})^2 / (1 - \rho_0^{1/2})^2. \quad (2)$$

In Figure 4 we plot  $\epsilon$  as a function of radius  $R$  using the measured value for  $\sigma$  and taking  $g = 1$  and  $g = 2$  as reasonable bounds for the backscatter gain. Note that  $g = 2$  corresponds to a rough sphere (or spheroid observed end-on) with an  $n = 1$  scatter law, while  $g = 1$  holds for a smooth sphere; backscatter gains for limb-bright scattering laws are not readily calculable, since the general form of the bistatic scattering function for the cosine backscatter law is undefined for  $n < 1$ . Also shown on this figure are the  $\epsilon$ -values for solid ice ( $0.9 \text{ g cm}^{-3}$ ), dry snow under natural pack conditions, solid rock, and rock powder

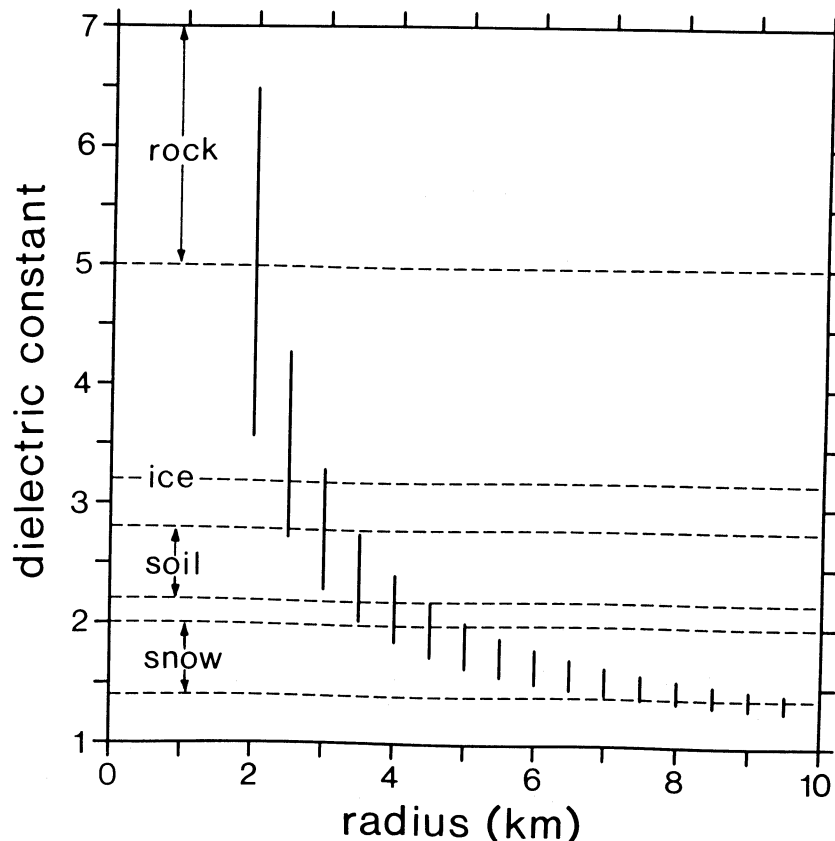


FIG. 4.—Surface dielectric constant vs. nucleus radius as calculated from the measured nucleus cross section and eqs. (1) and (2). The vertical bar covers the plausible range of values of the backscatter gain  $g$  ( $g = 1$  at top of bar,  $g = 2$  at bottom). The approximate ranges of dielectric constant for various surface compositions are also shown.



(Ulaby, Moore, and Fung 1981; Campbell and Ulrichs 1969; Evans 1969). Since the nucleus is very unlikely to have a reflectivity higher than that of solid ice, we can set a reasonably firm lower limit of 2.5 km for the radius. The upper size limit is less certain. The maximum radius assuming packed snow under Earth-like conditions is approximately 8 km. However, the windless, low-gravity conditions at the nucleus surface could result in snows of a lower density than is typically found on Earth, in which case the inferred radius would be larger than 8 km. This assumes, of course, that the snows are not "dirty." Admixtures of dust or rock would tend to increase the reflectivity and lower the inferred radius.

The only other size estimates for the IAA nucleus are those provided by thermal radiation measurements. These give size estimates falling roughly in the middle of the range of plausible values as inferred from the radar data. Hanner *et al.* (1985) give a radius estimate of  $5 \pm 0.6$  km based on observations of an infrared emission core on UT May 11.35. Altenhoff *et al.* (1983) reported a 1.3 cm radio continuum detection of 9 mJy on UT May 11.8, which, using the Rayleigh-Jeans law and an assumed nucleus temperature of 200 K, corresponds to a radius of 4.3 km. When compared with Figure 4, these radius estimates imply a low-reflectivity, low-density surface such as a deep layer of packed snow. Note that this argument is based on size estimates made on the assumption that the nucleus is spherical. Such a straightforward comparison of the radar and thermal continuum data may introduce errors if the nucleus is aspherical, especially if the rotational aspect is different for the various observations. Nevertheless, it is unlikely that the thermal data are consistent with a surface as highly reflective as solid ice or less reflective than lightly packed snow.

The limb-to-limb Doppler bandwidth  $f_0$  of a rotating spherical nucleus is given by

$$f_0 = \frac{8\pi Rv \sin i}{c\tau} = \frac{2.3R(\text{km}) \sin i}{\tau(\text{days})}, \quad (3)$$

where  $R$  is the radius,  $v$  is the radio frequency,  $\tau$  is the apparent rotation period, and  $i$  is the inclination angle of the rotation axis to the line of sight. The apparent rotation is the sum of the true (inertial) rotation and a pseudorotation from changing observing aspect. On May 11 the latter effect corresponded to an effective period of 9 days, which is sufficiently long to be ignored for our purposes. Using the measured  $f_0$  of 3.5 Hz, we have the result  $\tau(\text{days}) < 0.66R(\text{km})$ . Letting  $R = 5$  km and taking  $i > 45^\circ$  from Goldstein, Jurgens, and Sekanina (1984), we have the result  $2.3 < \tau < 3.3$  days. This relatively slow rotation is consistent with the fact that the Doppler spectrum shows very little time variation over the course of the Arecibo observations. To check for feature motion, we averaged the first and second halves of the observing period separately and compared the spectra. A spectral feature arising from a fixed structure with cometocentric latitude  $\eta$  on a spherical rotating nucleus would show a negative frequency shift  $\Delta f$  in a time  $\Delta t$  given by  $\Delta f = (\Delta t/\tau)\pi f_0 \cos \eta$ . For  $\tau = 3$  days this gives a shift  $\Delta f < 0.15$  Hz  $\text{hr}^{-1}$ . We found that the narrow central peak in the SC spectrum moved by less than 1 resolution cell (0.122 Hz) in 1 hour. We also checked the spectra for changes in the bandwidth  $f_0$ , which would be expected in the case of a rotating aspherical nucleus. The small measured bandwidth increase of 2.2%  $\text{hr}^{-1}$  is consistent with a slow rotation, although the extreme sensitivity of the inferred rotation period to the rotational phase and assumed model figure precludes our making a strong statement.

If an independent estimate of  $\tau$  were available, then one could turn the problem around and estimate the radius from  $\tau$  and  $f_0$ . However, it is clear from the above discussion that the Arecibo data cannot provide such an estimate, in part because of the short observing span, nor are there any available  $\tau$  estimates from other observations.

#### V. PARTICLES: SIZES AND ABUNDANCES

Perhaps the most interesting result of the IAA radar observations is the detection of the broad-band skirt echo. The spectral shape and polarization of this component indicate that the echo arises from scattering by large particles or grains in an extended debris cloud moving with the nucleus. This is only the second deep-space particle population, after Saturn's rings, to be detected with radar.

In this section we attempt to place constraints on the size of the particles responsible for the skirt echo; the radar polarization results are used to establish an upper size limit, while the total skirt mass, the nondetection of the skirt at X-band, and the radio continuum results are all used to establish a minimum effective particle size. We will then show that these results are consistent with the standard gas-drag theory for particle ejection from a comet nucleus. Finally, we will use this theory and the measured radar cross section to estimate the mass-loss rate in large grains and thereby determine the relative importance of large grains in the total nucleus mass loss.

##### a) Radar Polarization

The skirt echo is remarkable for being almost completely circularly polarized. The measured 1.5% depolarization is the lowest yet found for any solar system radar echo. By contrast, Saturn's rings yield radar echoes which are highly depolarized ( $\mu_c \cong 1$ ), a result which is most easily explained by invoking multiple scattering within a comparatively dense particle population (Cuzzi and Pollack 1978). It is easily shown that all the skirt particles would have to be confined to a region roughly 10 km in diameter in order for multiple scattering to account for the observed depolarization. Since (as is shown later) the skirt particles are dispersed over hundreds of kilometers, we can ascribe virtually all of the observed depolarization to single scattering from irregular particles in a very tenuous particle population.

The very low depolarization implies that the scattering particles are small compared with the radar wavelength. Larger particles yield low depolarization only if they are very nearly spherical or if they are made up of large plane facets which are much larger than a wavelength in size, shapes which we would reject as being unlikely for a cometary grain. Relatively simple theoretical calculations yield depolarization values of the order of 1% for aspherical particles in the Rayleigh limit  $a \ll \lambda$  (van de Hulst 1957), while experiments show that  $\mu_c = 0.3$ –0.5 for irregular particles with radius  $a = 2\lambda$  (Cuzzi and Pollack 1978). Most of the available depolarization results for the interesting Rayleigh-Mie transition region ( $a \sim \lambda/2\pi$ ) are based on calculations or experiments using spheroidal particles (Warner 1978; Allan and McCormick 1978; Mon 1982). The experimental data of Allan and McCormick (1978) are particularly useful; they give backscatter efficiency and circular depolarization as a function of size and orientation for oblate and prolate spheroids illuminated by a circularly polarized wave. We have used their data to calculate  $\mu_c$  as a function of particle size  $a$  for the case of random orientation (Fig. 5a). We have also calculated  $\mu_c$  as a function of  $a_m$  for the case of a continuous

particle size distribution  $n(a) \propto a^{-\alpha}$  with an upper size cutoff at  $a = a_m$  (Fig. 5b). In Figure 5c we show the backscatter efficiency  $Q_b(a)$  averaged over all orientations along with the corresponding values calculated for equivolume spheres using Mie theory. The details of the depolarization calculations and the Rayleigh approximations are given in Appendix A.

Figures 5a and 5b show that small irregular particles can give the required low depolarization. They also show that there is a sharp increase in depolarization with particle size near  $a = \lambda/2\pi$ , which is also the point where the backscatter efficiency  $Q_b$  departs from the steep  $a^4$  Rayleigh dependence. Figure 5a places an upper limit of 3 cm for the size of particles dominating the skirt echo if those particles are solid rock or ice, while Figure 5b places firm limits of  $a_m = 2$  cm (rock) and  $a_m = 5$  cm (ice) for the maximum particle size in a distribution. Inspection of Figure 5 suggests that the  $\alpha$ -value at which the depolarization shows a sharp rise tends to increase with decreasing dielectric constant  $\epsilon$ . Unfortunately, there are no available data for estimating the depolarization by particles with  $\epsilon < 2.5$ . If, for example, the skirt grains were low-density "snowballs," then the maximum grain size might well be in excess of 5 cm.

#### b) Total Mass in Particles

The steep falloff in backscatter efficiency in the Rayleigh regime can be used to set a lower bound to the effective particle size required to give the measured radar cross section of the skirt. If all particles are in the Rayleigh size regime ( $a_m < \lambda/2\pi$ ), then a power-law particle distribution with radar cross section  $\sigma$  will have a total mass given by (see Appendix B)

$$M \cong \frac{1}{3} \sigma \rho \left( \frac{\lambda}{2\pi} \right)^4 \left| \frac{\epsilon + 2}{\epsilon - 1} \right|^2 \left( \frac{7 - \alpha}{4 - \alpha} \right) \left[ 1 - \left( \frac{a_0}{a_m} \right)^{4-\alpha} \right] a_m^{-3}, \quad (4)$$

where  $\rho$  is the particle density and  $a_0$  is a minimum particle size. Assuming that the particles are solid ice ( $\rho = 0.9 \text{ g cm}^{-3}$ ,  $\epsilon = 3.3$ ) and letting  $\alpha = 3.5$ , we have the result  $M \cong 1.5 \times 10^{12} a_m^{-3} \text{ g}$ , where  $a_m$  is in centimeters. The mass of a 5 km radius nucleus of the same density is  $5 \times 10^{17}$ . Thus the skirt mass requirements pose no problem for  $a_m \sim 1$  cm. However, making  $a_m < 0.5$  mm results in a skirt mass approaching that of the nucleus itself, which is unreasonable if the nucleus is to be the source of the skirt particles. Later in this section we show that a more stringent constraint can be set on the basis of mass-loss rate.

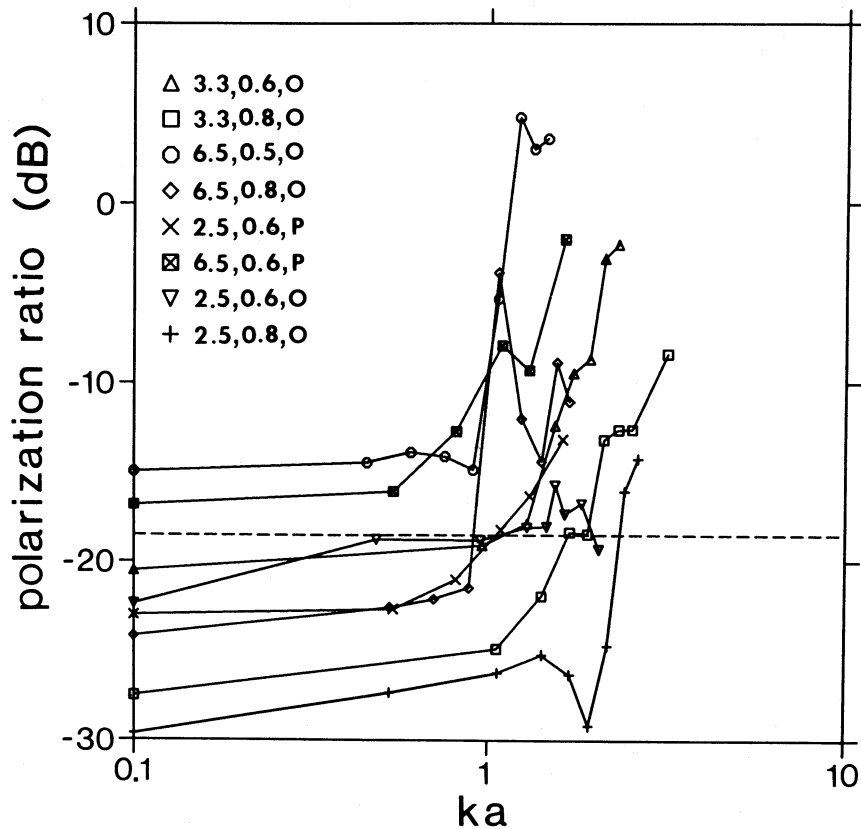


FIG. 5a

FIG. 5.—(a) Circular polarization ratio  $\mu_c$  as a function of particle size for a randomly oriented, single-scattering population of spheroids of axial ratio  $\eta$ . The size parameter is  $ka = 2\pi a/\lambda$ , where  $a$  is the equivolume radius. The curves were computed from eq. (A1) using the experimental data of Allan and McCormick (1978). The values at  $ka = 0.1$  are the Rayleigh limits computed from eqs. (A1), (A3), and (A4). The curves are for solid rock ( $\epsilon = 6.5$ ), solid ice ( $\epsilon = 3.3$ ), and a lower density material ( $\epsilon = 2.5$ ). The key gives  $\epsilon$ ,  $\eta$ , and the spheroid type (O = oblate, P = prolate). The measured polarization ratio of the skirt echo is also shown (dashed line). (b) Circular polarization ratio  $\mu_c$  as a function of maximum particle size for a randomly oriented population of spheroids, as in (a), with size distribution  $n(a) \propto a^{-3.5}$  and a maximum size  $a_m$ . The curves were computed using eq. (A2) and the data of Allan and McCormick (1978). (c) Backscatter efficiency  $Q_b$  as a function of particle size for a spheroid of equivolume radius  $a$ . The symbols are as in (a) and (b). The curves were computed by averaging the data of Allan and McCormick (1978) equally over all orientations. Also shown are the Mie curves for spherical ice and snow grains (solid curves) and the (orientation-averaged) Rayleigh approximation for an oblate spheroid with  $\epsilon = 6.5$ ,  $\eta = 0.5$  (dashed line).

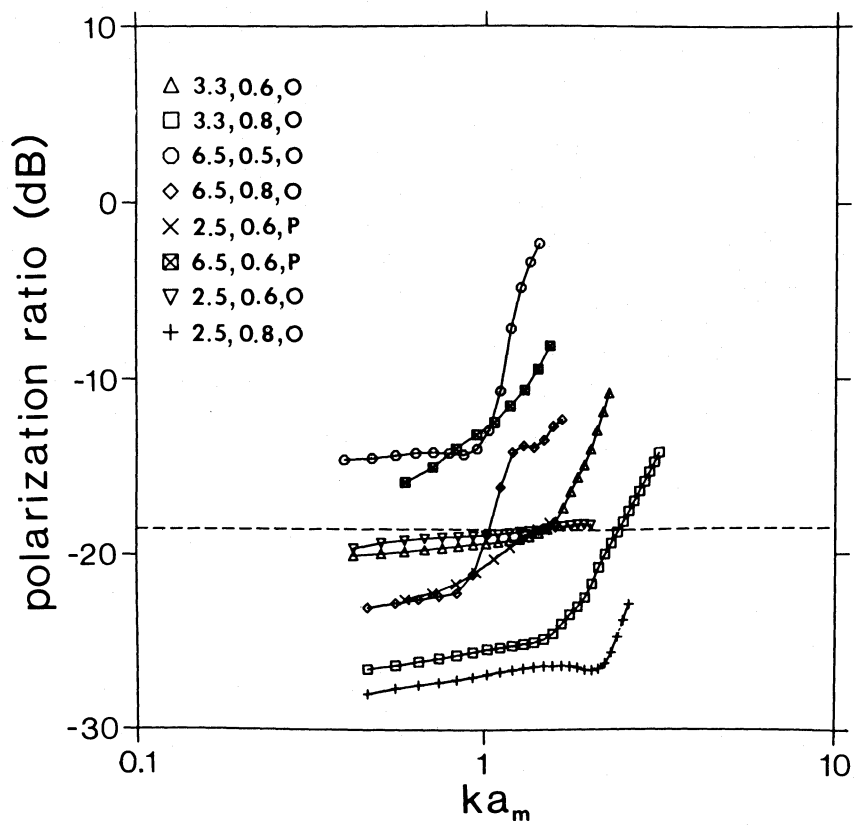


FIG. 5b

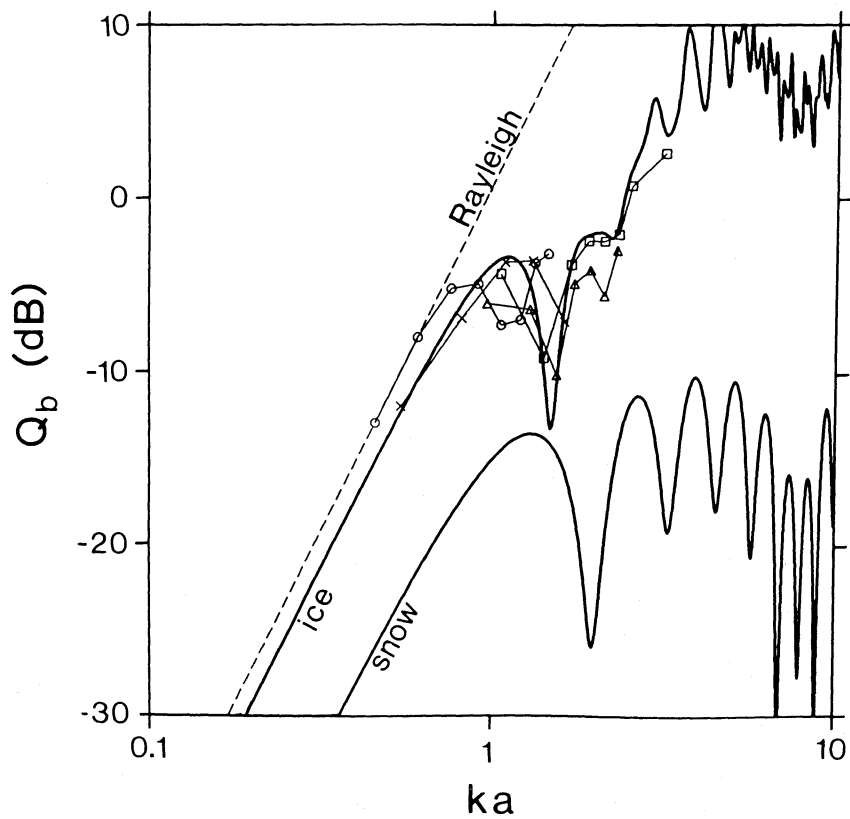


FIG. 5c

## c) X-Band Radar Nondetection

Given the  $\lambda^{-4}$  Rayleigh dependence of the backscatter efficiency, it is difficult to explain Goldstone's failure to detect a skirt echo at X-band ( $\lambda = 3.5$  cm) if the scattering particles are in the Rayleigh regime ( $a < \lambda/2\pi$ ) at both wavelengths. In Figure 6 we show the expected ratio  $\sigma_x/\sigma_s$  of the X- and S-band radar cross sections on the assumption that the Goldstone beam encompassed the same population of particles at both wavelengths. The cross sections were calculated for several types of particles using equation (B2) and using Mie theory to calculate  $Q_b$ . Also shown in Figure 6 is a line corresponding to the cross-section ratio at which the X- and S-band skirt echoes would have been equally detectable. Assuming the same radial velocity spread on May 11 and May 14 and assuming that the spectra at both wavelengths were smoothed to the same fraction of the skirt bandwidth, then the signal-to-noise ratio (S/N) obeys,

$$\frac{S}{N} \propto \frac{PG^2\lambda^{5/2}}{Td^4}, \quad (5)$$

where  $P$ ,  $G$ ,  $T$ , and  $d$  are the transmitted power, antenna gain, system temperature, and comet distance, respectively. Using  $P = 395$  kW,  $G = 62$  dB,  $T = 20$  K, and  $d = 5 \times 10^6$  km for the 12.9 cm observations, and  $P = 370$  kW,  $G = 71.5$  dB,  $T = 28$  K, and  $d = 11 \times 10^6$  km for the 3.5 cm observations (R. Jurgens 1987, private communication), then we estimate that the S- and X-band skirt echoes would have been equally detectable at Goldstone for  $\sigma_x/\sigma_s = 7.5$ .

For millimeter-size particles the curves in Figure 6 approach the Rayleigh value of  $(12.9/3.5)^4 = 182$ , and the skirt detection would have been 24 times stronger at X-band than at S-band. Even if the nucleus were unusually active in terms of particle

production just prior to the S-band observations of May 11, one can set a conservative lower limit of 1 cm for  $a_m$  based on the X-band nondetection of May 14. One has to make  $a_m > 2$ –3 cm in order for the X-band skirt echo to have a detectability which is comparable to or less than that of the S-band skirt, assuming that the particles are solid rocks or snowballs; the situation is different for solid ice spheres because of their unusual reflecting properties. Given the weakness of the Goldstone S-band skirt detection, it is likely that an X-band skirt would not have been detected if  $\sigma_x/\sigma_s < 2$ , that is, for  $a_m > 4$  cm. There are, of course, other ways to explain the lack of an X-band detection. One is to have the particle size distribution be flatter (lower  $\alpha$ ) than assumed in Figure 6, which would reduce the relative number of small particles. A second possible explanation is the fact that, although spheres and irregular particles have about the same backscatter efficiencies for size parameters  $2\pi a/\lambda = 1$ –2 (see Fig. 5c), Mie theory can overestimate the backscatter efficiencies of irregular particles for larger size parameters. This is at least true for solid ice spheres, which give 3–4 times stronger backscatter than aspherical ice particles for  $2\pi a/\lambda \cong 5$  (Warner 1978). A third consideration is the fact that the physical size of the Goldstone beam (at the comet) was a factor of 1.7 larger for the S-band observations of May 11 than for the X-band observations of May 14. However, this effect is mitigated by evidence suggesting that the particle cloud did not extend much beyond the limits of the relatively small Arecibo beam on May 11 (see § VIb). Finally, it is possible that the particle ejection rate was variable. Infrared and molecular-line observations (Feierberg *et al.* 1984; Brown, Cruikshank, and Griep 1985; Lutz and Wagner 1986) indicate outburst activity for IAA on May 10 and 11. Some of the particles produced in these outbursts could have evaporated or propagated outside the Goldstone beam by May 14.

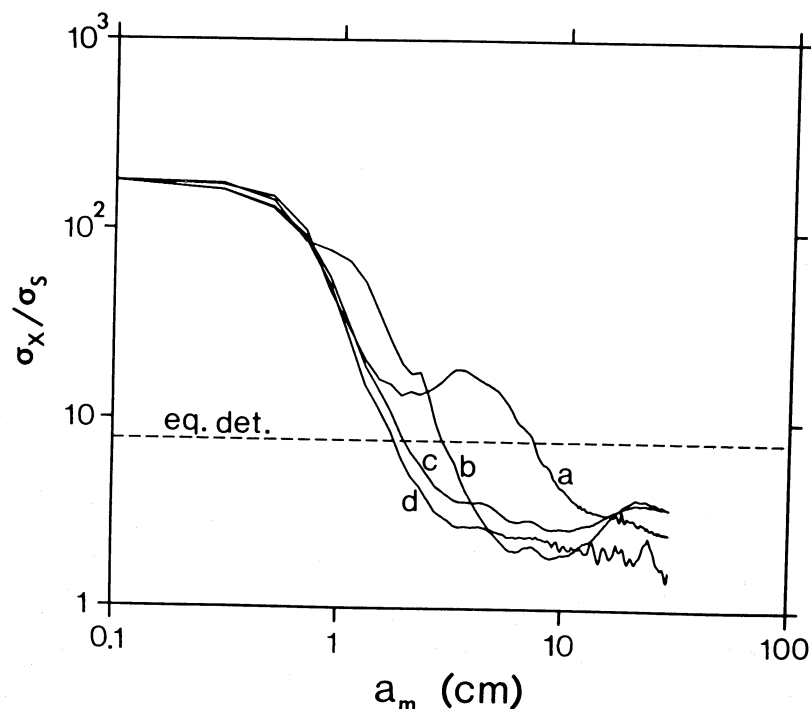


FIG. 6.—Curves of the expected ratio  $\sigma_x/\sigma_s$  of the Goldstone X-band ( $\lambda = 3.5$  cm) and S-band ( $\lambda = 12.9$  cm) radar cross sections of the skirt echo for several particle compositions: (a) ice,  $\epsilon = 3.3$ ; (b) rock,  $\epsilon = 6.5$ ; (c, d) snow,  $\epsilon = 1.44$ . The particle population spectral index  $\alpha$  is 3.5 for (a)–(c) and 3.0 for (d). The imaginary part ( $m_i$ ) of the refractive index is 0.03 for (b) and 0.01 for the rest. The level at which the X- and S-band echoes would have been equally detectable is also shown (dashed line).



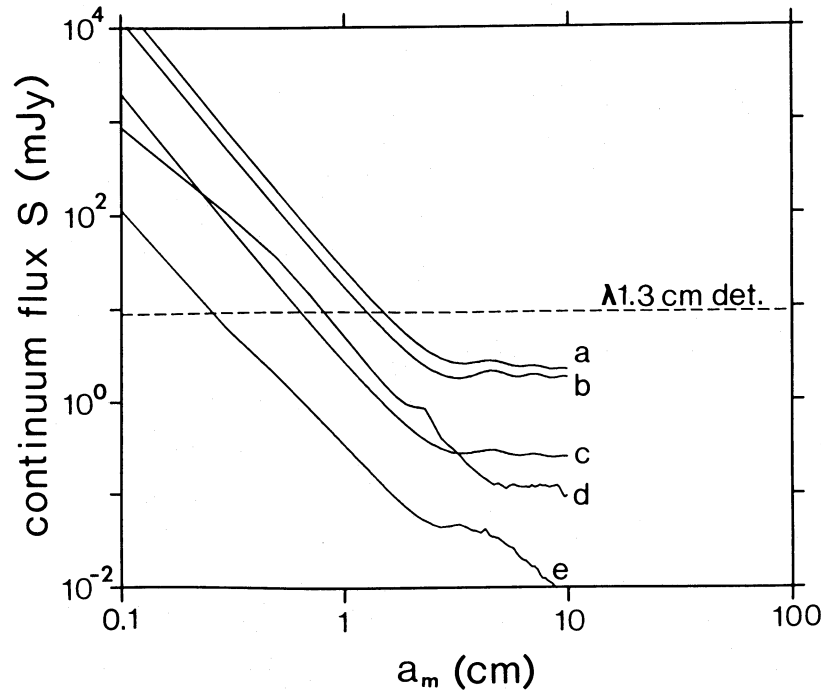


FIG. 7.—Curves of the expected 1.3 cm radio continuum flux density  $S$  vs. maximum grain radius  $a_m$  for several different compositions: (a, b) snow,  $m_i = 0.01$ ; (c) snow,  $m_i = 0.001$ ; (d) rock,  $m_i = 0.03$ ; (e) ice,  $m_i = 0.001$ . The calculations used a power-law particle population with a spectral index  $\alpha$  of 3.0 for (b) and 3.5 for the rest. The 1.3 cm flux measured by Altenhoff *et al.* (1983) is also shown (dashed line).

#### d) Radio Continuum Detection

Although the Bonn 1.3 cm radio continuum detection is consistent with thermal radiation from the nucleus (Altenhoff *et al.* 1983; de Pater *et al.* 1985; this paper, § IVb), the possibility of a significant contribution from large particles must be considered. The continuum flux density  $S$  from an optically thin particle population with size distribution  $n(a)$  is given by the following modified version of the Rayleigh-Jeans law (e.g., Walmsley 1985),

$$S = \frac{2\pi kT}{\lambda_c^2 d^2} \int_0^{a_m} n(a) Q_a(a; \lambda_c) a^2 da, \quad (6)$$

where  $T$  is the particle temperature,  $d$  is the comet distance,  $\lambda_c$  is the wavelength of the radio continuum observations, and  $Q_a(a; \lambda_c)$  is the absorption efficiency of a particle of radius  $a$  at wavelength  $\lambda_c$ . Letting  $n(a)$  be proportional to  $a^{-\alpha}$  and dividing equation (6) by equation (B2) to cancel the constant of proportionality in  $n(a)$ , we have

$$S = \frac{2kT\sigma}{\lambda_c^2 d^2} \frac{\int_0^{a_m} a^{2-\alpha} Q_a(a; \lambda_c) da}{\int_0^{a_m} a^{2-\alpha} Q_b(a; \lambda) da}. \quad (7)$$

Using  $\sigma = 0.8 \text{ km}^2$  from our radar results at wavelength  $\lambda$  (12.6 cm),  $\lambda_c = 1.3 \text{ cm}$ ,  $d = 0.33 \text{ AU}$ ,  $T = 200 \text{ K}$ , and calculating the efficiency factors  $Q_a$  and  $Q_b$  from Mie theory, we have calculated curves of  $S(a_m)$  for several different values of the complex refractive index (Fig. 7). The curves in Figure 7 assume that the particle cloud does not extend outside the Bonn beam (which was smaller than the Arecibo beam). If the cloud was larger than this, then the curves in Figure 7 should be lower by a factor of up to 4 (the ratio of the Arecibo to Bonn beam size). Note that, unless the particles have very low conductivity ( $m_i < 0.001$ ), making the maximum particle size  $a_m$  smaller

than about 0.3 cm gives a continuum flux density  $S$  which is higher than the measured 9 mJy regardless of the degree of beam filling. On the other hand, taking  $a_m > 2 \text{ cm}$  as implied by the X-band nondetection and mass-loss rate (see § Vf) gives a predicted flux density  $S$  which is much smaller than that observed. This suggests that most of the radio continuum emission came from the nucleus itself.

Walmsley (1985) has suggested that the radio continuum is due to a population of meter-size boulders in a 100 km diameter halo about the nucleus and comprising a total mass of a few percent of the nucleus mass. This suggestion can be discarded, since it would give a skirt echo with a much higher radar cross section and polarization ratio  $\mu_c$  than are observed. This hypothesis also appears to be somewhat artificial in light of the fact that the nucleus itself can probably account for most of the continuum emission.

#### e) Particle Ejection

The canonical model of cometary dust ejection, first proposed by Whipple (1951), postulates the dragging of particles by outflowing gases released in the sublimation of nucleus volatiles. This model, or refined versions of it, has been used in the study of the small (micron-scale) particles dominating the visible dust tail and infrared dust coma as well as the large (millimeter-scale) particles invoked to explain comet antitails (e.g., Finson and Probst 1968; Delsemme and Miller 1971; Sekanina 1974, 1981; Gary and O'Dell 1974; Wallis 1982). In its simplest form, this model assumes a uniform radial outflow of gas with constant thermal expansion velocity  $V_g$ . This leads to a familiar expression for the terminal ejection velocity  $V_t$  of a spherical particle of radius  $a$  (see, e.g., Gary and O'Dell 1974; Gambosi, Nagy, and Cravens 1986),

$$V_t = V_0(1 - a/a_m)^{1/2}, \quad (8)$$

where

$$V_0 = \left[ \frac{(3/2)V_g \dot{\mu} R}{a\rho} \right]^{1/2} \quad (9)$$

and

$$a_m = \frac{(9/16\pi)V_g \dot{\mu}}{R\rho_n \rho G}. \quad (10)$$

Here  $V_0$  is the terminal velocity in the absence of gravity,  $a_m$  is an upper size cutoff for the ejected particles, and  $(1 - a/a_m)^{1/2}$  is a gravity correction factor. Other quantities include the nucleus surface gas mass flux  $\dot{\mu}$ , the nucleus and particle mass densities  $\rho_n$  and  $\rho$ , the nucleus radius  $R$ , and the gravitational constant  $G$ . Note that because both gravity and gas drag are  $1/r^2$  forces in this model, any ejected particle ( $a < a_m$ ) is a free particle.

If we assume  $\rho = \rho_n = 1 \text{ g cm}^{-3}$ ,  $V_g = 0.28 \text{ km s}^{-1}$  ( $T = 200 \text{ K}$ ), and  $R = 5 \text{ km}$ , then we have  $V_0 = 1.45 \times 10^5 (\dot{\mu}/a)^{1/2} (\text{cm s}^{-1})$  and  $a_m = 1.5 \times 10^5 \dot{\mu} (\text{cm})$ . Using the gas mass-loss rate of  $6 \times 10^5 \text{ g s}^{-1}$  measured for IAA by Feldman, A'Hearn, and Millis (1984) and assuming uniform outgassing over the sunlit hemisphere gives  $\dot{\mu} = 4 \times 10^{-7} \text{ g cm}^{-2} \text{ s}^{-1}$ . This would give an  $a_m$  of only  $0.6 \text{ mm}$ , which is unreasonably low (see previous sections). Based on the high infrared temperature measured for the nucleus of IAA, Hanner *et al.* (1985) have argued that it is more likely that only about 1% of the total surface area of the nucleus was active (sublimating). This would give  $\dot{\mu} = 2 \times 10^{-5} \text{ g cm}^{-2} \text{ s}^{-1}$  and an  $a_m$  of  $3 \text{ cm}$ , which is consistent with the results of previous sections. For this  $\dot{\mu}$ -value a  $2 \text{ cm}$  radius particle would have a  $V_0$  of  $4.6 \text{ m s}^{-1}$  and a gravity-corrected velocity  $V_e$  of  $2.7 \text{ m s}^{-1}$ .

From the foregoing we conclude that the model of continuous particle ejection by gas drag offers a plausible mechanism for ejecting large grains with centimeter-scale maximum radii. In the following section (§ V f) we calculate the nucleus mass-loss rates implied by this model, and in § VI we consider the question of whether the ejection velocities are sufficient to explain the observed Doppler spread of the skirt echo.

#### f) Mass-Loss Rate

Using the particle ejection model, we have calculated the nucleus mass-loss rate required to give the measured radar cross section in particles. For isotropic ejection, the mass-loss rate  $\dot{M}$  is given by (see Appendix B)

$$\dot{M} = \frac{8}{3} \sigma \rho R \left[ \left( \frac{8\pi}{3} \right) \rho_n G \right]^{1/2} a_m^{9/2-\alpha} \left[ 1 - \left( \frac{a_0}{a_m} \right)^{4-\alpha} \right] \times \left[ \pi b(4-\alpha) \int_{a_0}^{a_m} \frac{a^{5/2-\alpha} Q_b(a)}{(1-a/a_m)^{1/2}} da \right]^{-1}, \quad (11)$$

where  $b$  is the distance subtended by the radar beam (half-width) at the comet. For the Rayleigh regime ( $a_m < \lambda/2\pi$ ) this reduces to (see Appendix B)

$$\dot{M} \cong \frac{(8/3)\sigma\rho R[(8\pi/3)\rho_n G]^{1/2} a_m^{-3} [1 - (a_0/a_m)^{4-\alpha}]}{\pi b(4-\alpha) C_Q B(1/2, 15/2-\alpha)}, \quad (12)$$

where  $B$  is the beta function and  $C_Q$  is the constant in the Rayleigh backscatter efficiency  $Q_b = C_Q a^4$  (see Appendix B). As was the case for the total mass  $\dot{M}$  (eq. 4),  $\dot{M} \propto a_m^{-3}$  for  $\alpha < 4$  and  $a_0 \ll a_m$ . For larger particles ( $a_m > \lambda/2\pi$ ) one must evaluate equation (11) numerically to get  $\dot{M}(a_m)$ . We show the results

of such calculations in Figure 8a for several values of  $\alpha$ . Here we have used Mie theory to calculate  $Q_b(a)$  and have assumed  $a_0 = 1 \mu\text{m}$ . Note that  $\dot{M}(a_m)$  turns over from the  $a_m^{-3}$  line for  $a_m > \lambda/2\pi$ . The levels of the  $\dot{M}$  curves are sensitive to  $\alpha$  for  $\alpha > 4$  but not for  $\alpha < 3.5$ , which simply reflects the fact that  $\dot{M}$  is dominated by the smallest particles for steep power laws ( $\alpha > 4$ ) and by the largest particles for shallow ones ( $\alpha < 3.5$ ). Also, the shape of the curves is rather insensitive to  $\alpha$ , which indicates that the local spectral index at large  $a$ -values is not very important. Therefore, we can take any of the low- $\alpha$  curves (say,  $\alpha = 3.0$ ) as giving the approximate mass-loss rate in large particles.

In Figure 8b we show the calculated  $\dot{M}(a_m)$  for  $\alpha = 3.0$  and several particle compositions: solid ice, solid rock, and a loosely packed snowball. Note that the  $\dot{M}$  curve for ice falls well below those of rock and snow for radii in excess of a few centimeters. This is a result of the unusual reflecting properties of large ice spheres; irregular ice grains would show a less marked effect. For smaller sizes ( $a_m < 6 \text{ cm}$ ) the curves for solid ice and rock track each other fairly closely. The lightweight snowball, on the other hand, gives  $\dot{M}$ -values which are roughly 3 times higher than those for the denser particles. In general, one expects  $\dot{M}$  to increase with decreasing particle density  $\rho$  for a given composition. The Rayleigh "mixing formula" (Evans 1969; Campbell and Ulrichs 1969) has  $C_Q \propto \rho^2$ , so that from equation (12) we have the result  $\dot{M} \propto \rho^{-1}$ .

In Figure 8b we plot a line showing the gas mass-loss rate inferred from OH observations by Feldman, A'Hearn, and Millis (1984). Note that the particle mass-loss rate is comparable to or less than the gas loss rate for particle radii less than  $10 \text{ cm}$ . Thus our gas-drag ejection mechanism does not appear to be heavily mass-loaded. If, however, one were to have  $a_m < 1 \text{ cm}$ , then the gas would be heavily mass-loaded. Such a condition is not disallowed, although it would result in somewhat lower ejection velocities. We also note the fact that the curves in Figure 8b were calculated on the assumption that sublimation of the ejected particles was unimportant. If this is not the case, then the  $\dot{M}$  curves will tend to underestimate the mass loss required to give the measured radar cross section. Also, Feldman's gas loss rate would overestimate the gas flux at the surface if their measurement included gas produced in the sublimation of ejected grains. Both of these effects would conspire to increase the mass-loading of the gas.

We can use the results in Figure 8 to compare the inferred mass-loss rates for large grains with those for the smaller dust particles. Hanner *et al.* (1985) estimated the total mass-loss rate in particles to be between  $9 \times 10^4$  and  $2 \times 10^5 \text{ g s}^{-1}$  for assumed  $\alpha$ -values between 4.7 and 4.2, respectively. These rates were based on extrapolation to centimeter-size particles, although the assumed power-law slope was sufficiently steep to ensure that the small dust particles would represent a large fraction of the quoted loss rates. Walker *et al.* (1984) arrived at a comparable ( $2 \times 10^5 \text{ g s}^{-1}$ ) loss rate in dust based on infrared observations with the IRAS satellite. We plot the two loss-rate values of Hanner *et al.* (1985) in Figure 8b. Comparing these with our curves in Figure 8b indicates that the mass-loss rate in large grains is roughly comparable to that for the smaller dust particles. A comparison of the  $\alpha = 4.2$  curve in Figure 8a with the Hanner line for the same  $\alpha$  shows that the large grains are roughly a factor of 15 more abundant than is predicted by Hanner's extrapolated particle production distribution  $\dot{n}(a)$ . Since this extrapolation was made over approximately 3.5 decades in particle size, then one requires a flatter

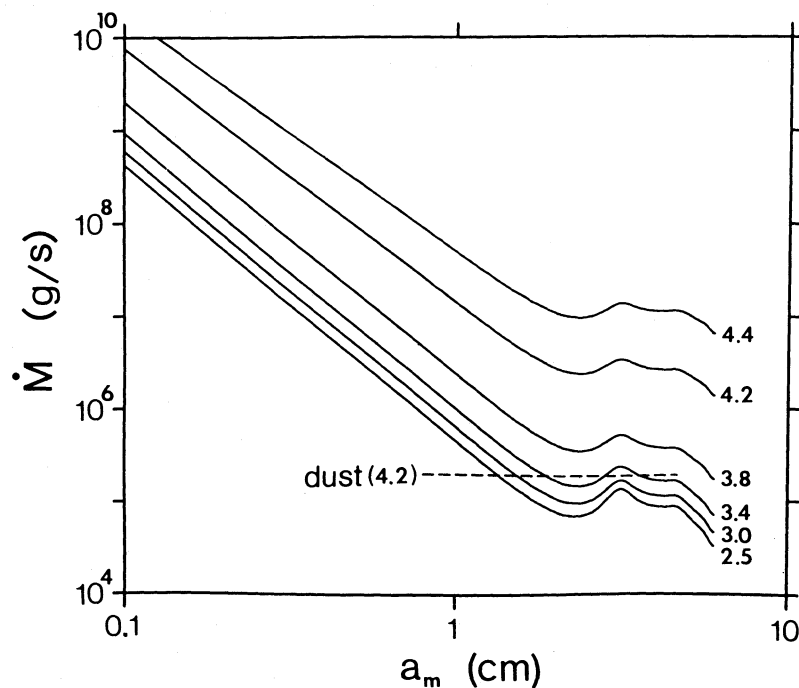


FIG. 8a

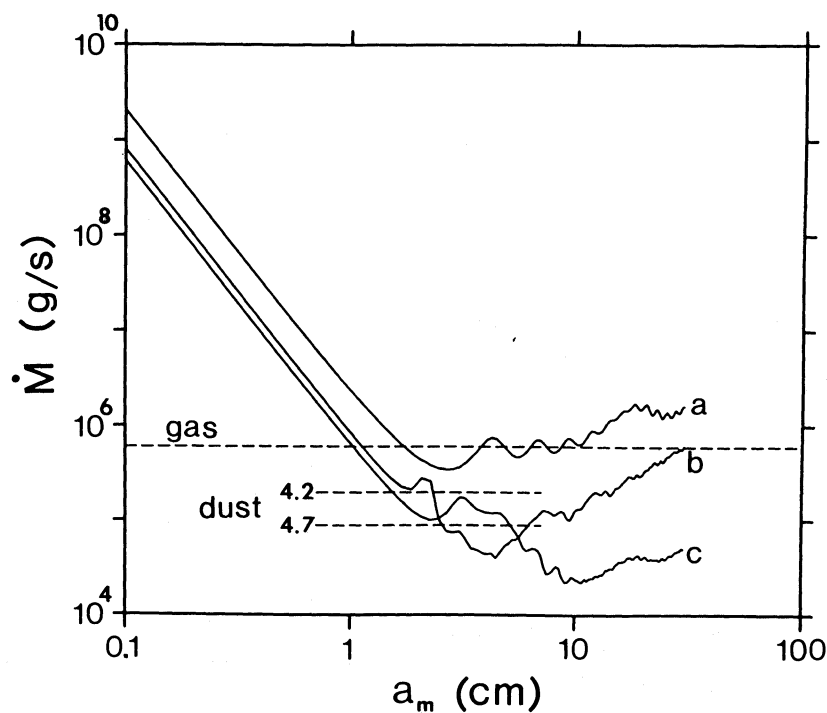


FIG. 8b

FIG. 8.—(a) Curves of total particle mass-loss rate  $\dot{M}$  vs. maximum particle size  $a_m$  for various values of the particle production spectral index  $\alpha$ . These curves have been calculated using Mie theory and eqn. (11) for  $1 \text{ g cm}^{-3}$  ice particles with assumed minimum size  $a_0 = 1 \text{ } \mu\text{m}$ . The dashed line shows the  $\dot{M} = 2 \times 10^5 \text{ g s}^{-1}$  value inferred by Hanner *et al.* (1985) from an extrapolation of their infrared-derived dust-particle concentrations to centimeter scales; they assumed  $\alpha = 4.2$ ,  $\rho = 1 \text{ g cm}^{-3}$ , and  $\dot{\mu} = 2 \times 10^{-5} \text{ g cm}^{-2} \text{ s}^{-1}$ . (b) Curves of total particle mass-loss rate  $\dot{M}$  vs. maximum grain radius  $a_m$  for several compositions: (a) snow,  $\rho = 0.3 \text{ g cm}^{-3}$ ; (b) rock,  $\rho = 3 \text{ g cm}^{-3}$ ; (c) ice,  $\rho = 1 \text{ g cm}^{-3}$ . These curves were calculated using Mie theory and eq. (11) with  $\alpha = 3.0$ . The dashed lines show the  $6 \times 10^5 \text{ g s}^{-1}$  mass-loss rate in gas as given by Feldman, A'Hearn, and Millis (1984) and the particle mass-loss rates estimated by Hanner *et al.* (1985) from extrapolations of dust-content measurements with  $\alpha = 4.2$  and  $4.7$ .

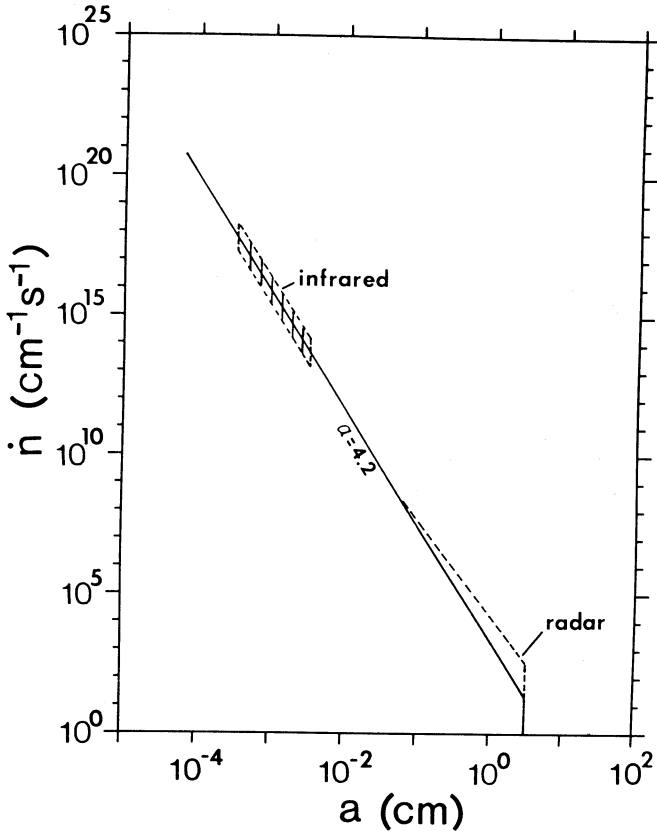


FIG. 9.—Particle production size distribution  $\dot{n}(a)$  estimated by Hanner *et al.* (1985) from an  $\alpha = 4.2$  extrapolation of their infrared data to centimeter sizes (solid line). The hatching indicates the size regime to which the infrared observations are sensitive. The dashed line shows the large-particle “excess” (relative to the IR extrapolation) required by the radar observations, for an assumed spectral index (at large sizes) of  $\alpha = 3.5$ . Note that a steeper ( $\alpha = 3.8$ – $3.9$ ) dashed line would intersect the hatched region when pivoted about the radar-inferred  $\dot{n}$  level at  $a_m = 3$  cm.

$\dot{n}(a)$  with  $\alpha = 3.8$ – $3.9$  in order to give the observed abundance of centimeter-size grains. In Figure 9 we show the  $\dot{n}(a)$  function deduced by Hanner *et al.* (1985) and the large-grain excess (relative to Hanner’s extrapolation) required to explain the radar results. Note that only the largest grains contribute to the radar echo, so that a two-component power-law model for  $\dot{n}(a)$  with  $\alpha < 3.9$  for the grains would be consistent with both radar and infrared results.

## VI. PARTICLES: SPECTRUM MODELING AND SPATIAL DISTRIBUTION

In the previous section we showed that the radar cross section and polarization of the skirt echo were consistent with backscattering from centimeter-size grains ejected by gas drag from the nucleus. In this section we will establish (1) whether the *shape* of the skirt Doppler spectrum is also consistent with this model and (2) the extent to which one can determine the spatial distribution of the particles from the spectrum.

### a) Doppler Spectrum Evaluation

Here we derive an expression for the Doppler spectrum  $\sigma(f)$  which one would expect to measure given the assumed particle ejection model. In Appendix C we show that the Doppler fre-

quency (relative to the nucleus) of a particle of size  $a$  emitted in direction  $\hat{e}$  at time  $t$  prior to the observation time  $t_0$  is given by

$$f(a; t, \hat{e}) = g(t, \hat{e}) V_L(a) \\ = g(t, \hat{e}) [(8/3)\pi\rho_n G]^{1/2} R a^{-1/2} (a_m - a)^{1/2}, \quad (13)$$

where

$$g(t, \hat{e}) = -\frac{2v}{c} \{ \hat{v}_{pc} \cdot \hat{r}_{ce} + r_{ce}^{-1} \\ [\hat{v}_{ce} - (v_{ce} \cdot \hat{r}_{ce})\hat{r}_{ce}] \cdot \hat{v}_{pc}(t_0 - t) \}. \quad (14)$$

Here the subscripts “pc” and “ce” denote the velocity and position vectors of the particle relative to the comet nucleus and of the nucleus relative to the Earth, respectively, and carets denote unit vectors. The solution of  $\hat{v}_{pc}$  in terms of the emission parameters  $\hat{e}$ ,  $t$  is also given in Appendix C. Equation (14) is easily modified to give a first-order correction for the solar “tidal” force across the extended particle cloud (Appendix C). We have, however, ignored radiation pressure, which has a relatively small effect on the model skirt spectrum (see Appendix C).

The first term inside the braces in equation (14) is the component of Doppler offset due to particle motion relative to the nucleus (“velocity component”), whereas the second term is the Doppler component from the geometrical projection of the particle’s spatial separation vector from the nucleus (“spatial component”). This convenient result (see Appendix C) will allow us to place some constraints on the size of the particle cloud based on the observed spread of the skirt spectrum.

The model Doppler spectrum  $\sigma(f)$  can be approximated as the sum of spectral contributions from discrete particle emission times and directions, i.e.,

$$\sigma(f) = \sum_i \sum_j \sigma(f; t_i, \hat{e}_j) \Delta\Omega \Delta t, \quad (15)$$

where  $\sigma(f; t_i, \hat{e}_j)$  is the spectral contribution per unit solid angle  $\Omega$  per unit time  $t$ . Since  $f$  in equation (13) is a monotonic function of particle radius  $a$ , we have the following result:

$$\sigma(f; t, \hat{e}) = \left\{ \sigma(a; t, \hat{e}) \left/ \left| \frac{d}{da} [f(a; t, \hat{e})] \right| \right\} B(\theta), \quad (16)$$

where

$$\sigma(a; t, \hat{e}) = \pi a^2 Q_b(a) \dot{n}(a; t, \hat{e}). \quad (17)$$

Here  $B(\theta)$  is a factor ( $\leq 1$ ) accounting for the finite antenna beam size, where  $\theta$  is the angular separation between nucleus and particle as observed from Earth. The denominator of equation (16) can be found from differentiating equation (13). Also,  $\dot{n}(a; t, \hat{e})$  is the distribution for particle production per unit solid angle per unit time. The model spectrum is then specified by substituting equation (16) in equation (15).

### b) Skirt Spectrum Modeling Results

Using equations (13)–(17), we have numerically computed model Doppler spectra for comparison with the observed skirt spectrum. The nucleus gravity was specified by assuming  $\rho = 1$  g cm<sup>-3</sup> and  $R = 5$  km. For the production rate distribution  $\dot{n}(a)$  we assumed an  $\alpha = 3.5$  power law, and, unless otherwise noted, an upper size cutoff  $a_m = 3$  cm. For  $Q_b(a)$  we used the values for irregular ice grains. The summation in equation (15) assumed a constant production rate  $\dot{n}$  over a period beginning as early as 30 days before the observations, during which time



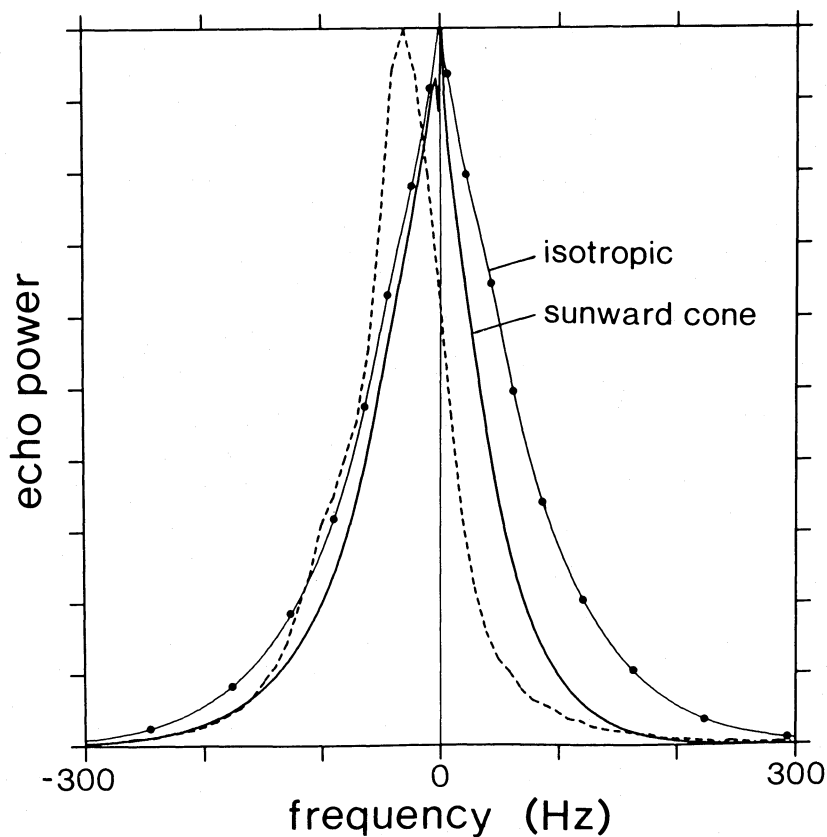


FIG. 10a

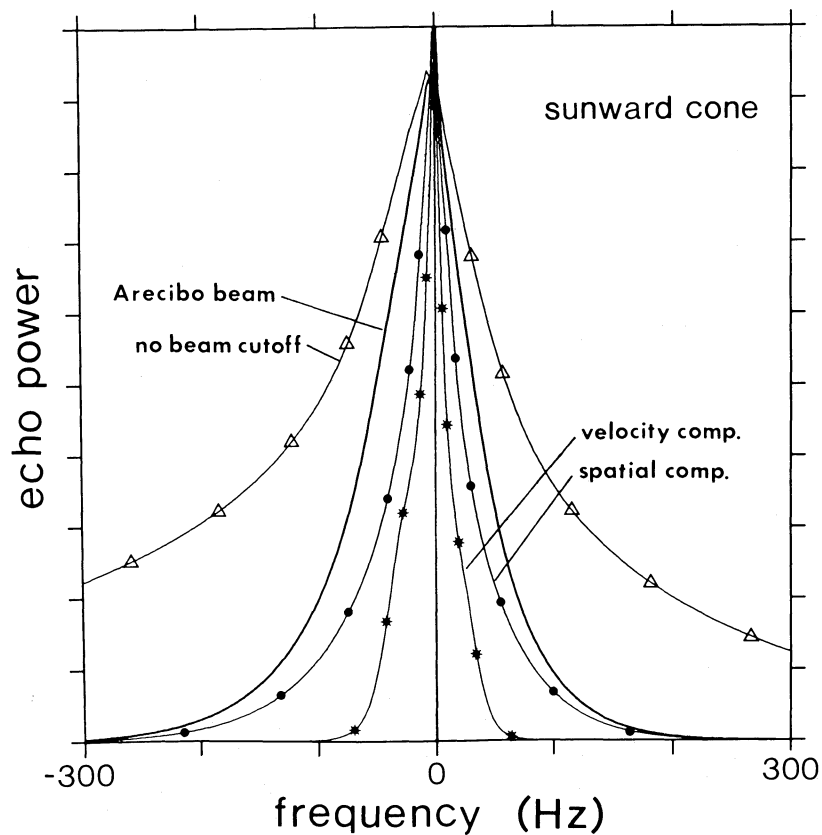


FIG. 10b

FIG. 10.—(a) Model skirt spectra for a  $120^\circ$  wide sunward-centered ejection cone and for isotropic particle ejection. In both cases the particle ejection rate is constant over a 30 day period ending on May 11. The model curves are evaluated numerically at a frequency interval of 2.5 Hz. Also shown is the observed skirt spectrum from the Arecibo radar observations (*dashed curve*). (b) Model spectrum for the  $120^\circ$  wide ejection cone of (a), along with the same spectrum broken down into its “velocity” and “spatial” Doppler components. Also shown is the same model spectrum with the effect of the Arecibo beam cutoff removed.

the comet's heliocentric distance decreased from 1.2 to 1.0 AU. Longer periods were not of interest, since our model had most grains moving outside the Arecibo beam within a week of ejection.

In Figure 10a we show the computed model spectrum for the case of isotropic particle ejection over a 30 day period. Note that this model spectrum is significantly broader than the observed spectrum and, unlike the observed spectrum, is symmetric about zero Doppler frequency. A more plausible model for a slowly rotating comet such as IAA would have preferential ejection in the solar direction due to enhanced sublimation over the sunlit hemisphere. Visual and infrared observations of the inner coma do, in fact, show a broad dust fan directed toward the Sun (Feierberg *et al.* 1984; Hanner *et al.* 1985; Brown, Cruikshank, and Griep 1985; Oliverson, Hollis, and Brown 1985; Storrs *et al.* 1986). In Figure 10a we include the model spectrum for the case in which there is uniform particle ejection over a  $120^\circ$  wide cone of emission centered on the Sun direction. Note that the sunward-ejection model gives a spectrum which is narrower than the isotropic spectrum and which is offset toward negative frequencies, in better agreement with the observed spectrum.

In Figure 10b we show the model spectrum for the sunward-ejection case broken down into its velocity and spatial components (see § VIa). Note that the spatial component dominates the spectral width, especially in the high-frequency wings. Hence, the breadth of the skirt spectrum can provide information on the size of the grain cloud. Also shown in Figure 10b is the model spectrum for the case where the cutoff

effect of the finite beam size has been removed. This spectrum is very broad, which indicates that the shape and spread of the spectral wings should be beam-dominated if the grain cloud extends beyond the edge of the radar beam.

The simple sunward-ejection model shown in Figure 10 still does not adequately reproduce the observed spectral shape and offset. The average negative offset can be increased by rotating the emission-cone direction below the comet orbit plane or toward the direction of comet motion, while reproducing the shape and offset of the peak of the spectrum requires that a portion of the particle emission be concentrated in a relatively narrow cone or "jet." An offset of the emission from the precise solar direction is a likely consequence of comet rotation due to the combined effects of thermal time lags in subsolar sublimation and the nonnegligible (tenths of a meter per second) initial tangential velocities at the nucleus surface. After testing a large number of emission geometries, we arrived at the provisional model giving the skirt spectrum shown in Figure 11. This model has 65% of the particle emission in a  $140^\circ$  wide cone of ejection and the remaining 35% in a narrow  $30^\circ$  cone. The centroids of these concentric emission cones were assumed, at all times, to be directed toward the Sun (as viewed along a normal to the orbit plane) but rotated by  $25^\circ$  below the orbit plane (where "below" is defined as the direction opposite the orbital angular momentum vector). This particle ejection direction agrees well with the observed orientation of the comet's dust fan in the inner coma. This can be seen from Figure 12, which shows the Sun direction and our deduced ejection direction projected on maps of visual and

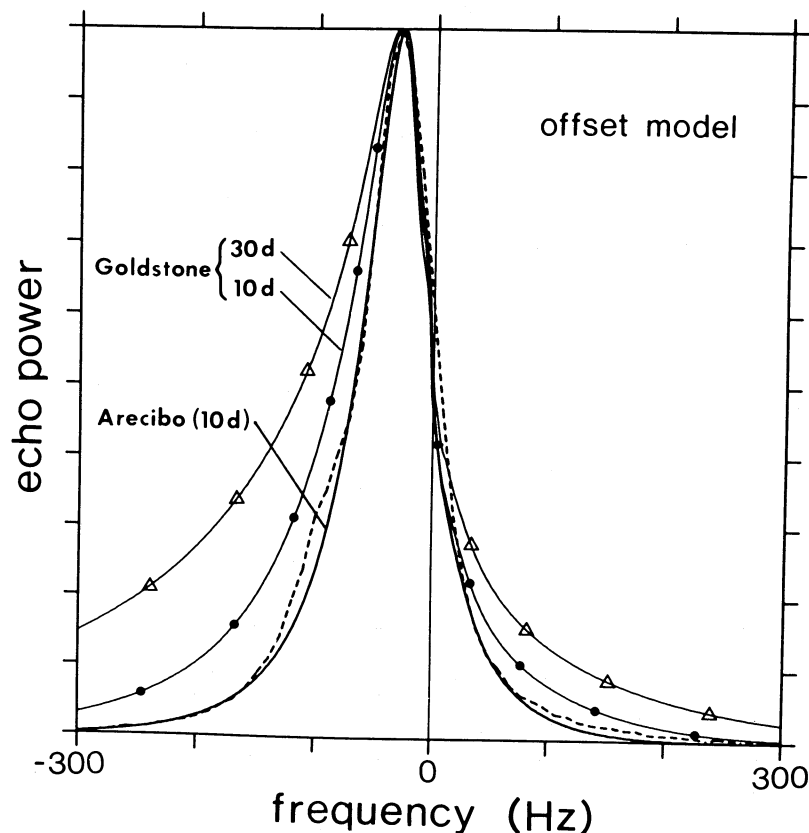


FIG. 11.—Model skirt spectrum for a mean ejection direction offset by  $25^\circ$  from the Sun direction and with a particle flux which is nonuniform over the ejection cone (see text for details). Model spectra are shown for Arecibo (10 day ejection period) and Goldstone (10 and 30 day ejection periods). Also shown is the observed Arecibo skirt spectrum (dashed curve).

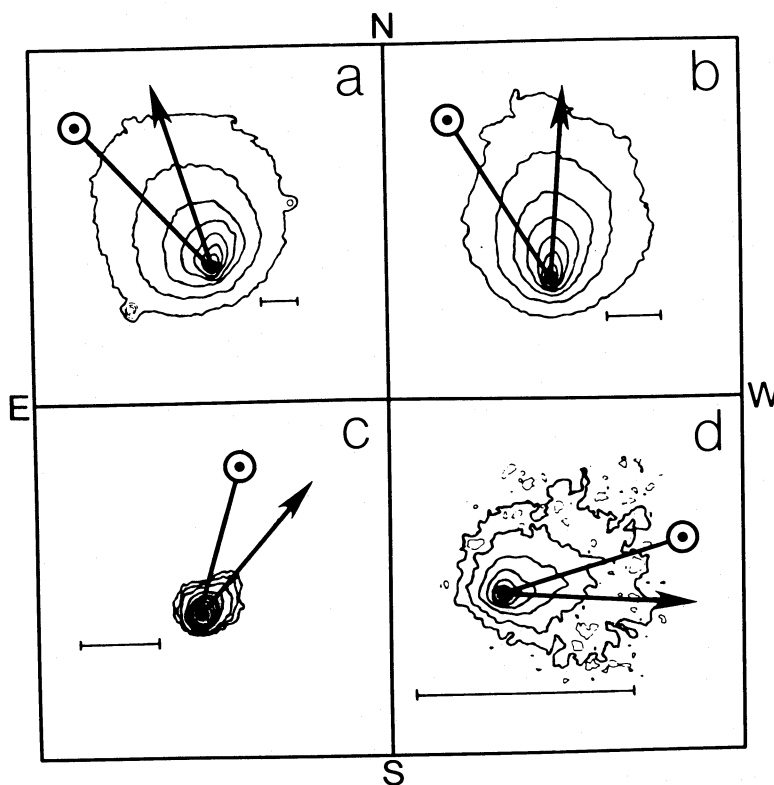


FIG. 12.—Contours of visual and near-visual continuum brightness for the inner coma of IAA at four different (UT) epochs: (a) May 8.60, (b) May 9.62, (c) May 10.25, (d) May 11.27. The data are from Storrs *et al.* (1986) (red continuum for May 8.60 and May 9.62 and infrared continuum for May 11.27) and Oliverson, Hollis, and Brown (1985) (blue continuum for May 10.25). Also shown are the sky projections of the comet-Sun vector (heavy circled dot) and of the center of the radar-inferred ejection fan (arrow) as given by the model used in Fig. 11. The scale corresponding to 1000 km (bar) is given for each epoch.

infrared continuum emission from dust (Storrs *et al.* 1986; Oliverson, Hollis, and Brown 1985). Note that our ejection direction approximately reproduces the observed offset of the dust emission contours from the solar direction during May 8–11. Our emission direction is consistent with the nucleus rotation geometry deduced by Storrs *et al.* (1986), which has the spin axis roughly perpendicular to the comet-Sun line and the spin-axis north pole pointing away from the direction of the comet's forward motion.

Figure 11 shows that a particle ejection period of 10 days (beginning 10 days before the observations) will essentially fill the Arecibo beam (1100 km half-width) but not the 3.3 times larger Goldstone beam. Although the Goldstone skirt echo is very noisy, a comparison between Figure 2c and 11 suggests that we can discard the possibility that the large grains extend out to the edge of the Goldstone beam. This is supported by the fact that Arecibo and Goldstone measured comparable radar cross sections for the skirt echo. By integrating under our model spectrum  $\sigma(f)$ , we conclude that the Goldstone cross section should be a factor of 2.2 higher than the Arecibo cross section for a 30 day ejection period. Lowering the ejection period to 7 days reduces this factor to 1.26 and still gives a good match between the observed and model skirt spectra. However, reducing the period to less than about 3 days results in a significant narrowing of the model spectrum as the beam filling decreases and the spatial term in the Doppler offset becomes less important. Thus the ejection model of Figure 11 requires that the Arecibo beam be substantially filled to compensate for the low ( $\sim 3 \text{ m s}^{-1}$ ) ejection velocities. The filled-

beam requirement can, of course, be relaxed by going to a model giving higher ejection velocities. The obvious model is one in which the grain cutoff size  $a_m$  is large (say,  $\sim 10 \text{ cm}$ ), as could be the case if the grains are low-density snowballs. Since the backscatter efficiency curve  $Q_b(a)$  should remain flat for grain sizes greater than 3 cm, then much of the scattering will come from the relatively fast grains with sizes near the Mie turnover ( $a \sim 2\text{--}3 \text{ cm}$ ). Even in this case some contribution to the Doppler spread from beam filling is required and, given the higher velocities, one would expect the beam to fill rather rapidly in any event.

The fact that most of the large grains appear to be confined to a radius of  $\sim 1000 \text{ km}$  suggests a highly variable grain emission rate, a limited grain lifetime, or both. The rate of decrease of heliocentric distance was too slow (0.2 AU between April 11 and May 11) to produce a rapid increase in particle production in early May through the normal heliocentric variation in sublimation rate. On the other hand, IAA did show highly variable activity, with major outbursts in dust production being seen on May 10 and 11 (Feierberg *et al.* 1984; Brown, Cruikshank, and Griep 1985; Lutz and Wagner 1986). Recent outbursts such as these might produce a large concentration of grains within a few hundred kilometers of the nucleus and, if associated with the activation of a collimated jet, could give the concentrated emission component required by our model. The alternative explanation for grain concentration, that the grains have a limited lifetime on the scale of several days, is plausible if the grains consist of evaporating ice. This possibility was first suggested in the "icy-grain halo" theory of Delsemme and Miller

(1971). Although the sublimation rate depends on the "dirtiness" of the icy grain, a lifetime of one week for a 1 cm grain is reasonable (Hanner 1981; de Pater *et al.* 1985).

#### VII. SUMMARY AND CONCLUDING REMARKS

The radar data indicate that the nucleus of comet IRAS-Araki-Alcock is a single solid object a few kilometers in size. The inferred diameter depends on surface composition, varying between 5 km for a solid-ice surface to 16 km for a surface of loosely packed snow. If the diameter ( $\sim 10$  km) inferred from thermal emission data is correct, then a low-density, low-reflectivity surface such as a packed snow layer is called for. The nucleus appears to be a very rough object on scales of several meters or more and, hence, is probably similar to many asteroids in its surface structure. The Doppler bandwidth of the nucleus indicates a relatively long rotation period (2–3 days), which is consistent with the observed lack of variation in the nucleus echo over the course of the Arecibo observations.

The radar results provide unambiguous evidence for the existence of a cloud of large grains moving with the nucleus. We have shown that the broad-band (skirt) echo must be dominated by grains with sizes of several centimeters. A simple gas-drag theory is capable of explaining the ejection of such large grains from the nucleus. The size of the particle cloud is of the order of  $10^3$  km, which is roughly the volume filled by ejected grains moving at meter per second velocities for several days. The radar data are consistent with preferential ejection from the sunlit hemisphere, although the mean ejection direction shows a definite offset from the solar direction. The direction of the grain emission fan agrees well with that of the smaller (micron-size) dust particles in the inner coma, which lends support to the notion that the large (centimeter-size) grains are part of a general distribution of particles ejected from the nucleus by subsolar sublimation. The radar cross section of the skirt echo can be explained using a particle size distribution (for production) which is extrapolated from the number densities of micron-size dust particles using a power-law index of 3.8–3.9. Although this is shallower than the  $\alpha > 4$  power laws customarily assumed in estimating large-grain production, the implied large-particle "excess" poses no problems for the mass-loss budget of the nucleus. It does, however, indicate that large (millimeter- to centimeter-size) grains account for a significant fraction of the total mass loss in particles from the nucleus.

An unexpected irony of the radar results for IAA is that they

have permitted us to make more detailed inferences about the ejected particles than about the nucleus itself. Most of the ambiguities with regard to the nucleus could have been resolved had radar-ranging information been obtained. Thus, a high priority should be given to making high-resolution ranging observations of future comet encounters should such opportunities arise. The recent acquisition of a continuous fast-sampling capability at Arecibo Observatory was largely motivated by this consideration.

Our interpretation of the particle echo suggests that, in retrospect, the skirt echo detection should not have come as a surprise. The fact that the nucleus and skirt cross sections are comparable suggests that particle echoes should be searched for in any future radar observations of comets. Given that IAA was a relatively dust-poor comet, it is conceivable that a "bright" (active) comet could give a significantly higher radar cross section from particles than from the nucleus. This does not necessarily imply that the particle echo from such a comet would be more easily detectable than the nucleus echo, since the detectability of a spectral feature in noise worsens as the square root of the feature bandwidth. We may, however, already have found an early example of just such a case. Arecibo radar observations of comet Halley during its 1985 inbound approach (0.62 AU distance) gave a weak detection in the form of a broad Doppler feature with a  $32 \text{ km}^2$  radar cross section (Campbell, Harmon, and Shapiro 1989). Such a feature is very difficult to reconcile with a nucleus echo but is easily explained as a particle cloud echo given Halley's relatively high degree of activity. One might expect to make comet particle detections at even larger distances if the nucleus activity is sufficiently high to compensate for the (distance) $^{-4}$  dependence of radar detectability. For example, a bright Sun-grazing comet might be detectable near perihelion, when the particle production rates would be expected to be very high.

We wish to thank the staffs of the Arecibo Observatory (NAIC) and the Harvard-Smithsonian Center for Astrophysics, as well as A. Forni of MIT Lincoln Laboratory, for their support of these observations. The National Astronomy and Ionosphere Center is operated by Cornell University under a cooperative agreement with the National Science Foundation (NSF) and with support from the National Aeronautics and Space Administration. One of us (I. I. S.) was supported in part by a grant from the NSF.

#### APPENDIX A

##### DEPOLARIZATION BY SPHEROIDS

Any asphericity in the scattering particle will result in a backscattered wave which is partially depolarized. We model a particle as a spheroid whose axis of symmetry makes an angle  $\theta$  with respect to the line of sight. If one has a population of single-scattering particles of radius  $a$  and random orientation  $\theta$ , then the total polarization ratio will be

$$\mu_c(a) = \frac{\int_0^{\pi/2} \mu_c(a, \theta) Q_b(a, \theta) \sin \theta d\theta}{\int_0^{\pi/2} Q_b(a, \theta) \sin \theta d\theta}, \quad (\text{A1})$$

where  $\mu_c(a, \theta)$  and  $Q_b(a, \theta)$  are the polarization ratio and backscattering efficiency as a function of particle size and orientation. Equation (A1) was used to compute the curves shown in Figure 5a.

The corresponding equation for the case of a continuous particle size distribution  $n(a)$ , where  $n(a) = 0$  for  $a > a_m$ , is given by

$$\mu_c(a_m) = \frac{\int_0^{a_m} \int_0^{\pi/2} \mu_c(a, \theta) Q_b(a, \theta) n(a) a^2 \sin \theta d\theta da}{\int_0^{a_m} \int_0^{\pi/2} Q_b(a, \theta) n(a) a^2 \sin \theta d\theta da} \quad (\text{A2})$$



In general  $\mu_c(a, \theta)$  and  $Q_b(a, \theta)$  must be determined from complex calculations or experiments. However, in the Rayleigh limit  $a \ll \lambda$  they reduce to simple forms for spheroids (Allan and McCormick 1978). The backscatter efficiency for a spheroid of dielectric constant  $\epsilon$ , eccentricity  $e$ , and equivalent (equivolume) radius  $a$  is given by

$$Q_b(a, \theta) = \frac{16(2\pi a/\lambda)^4}{|2K - T|^2} \left| 1 - \frac{3T}{4(K + T)} \sin^2 \theta \right|^2. \quad (\text{A3})$$

The corresponding equation for the circular polarization ratio is

$$\mu_c(a, \theta) = \mu_c(\theta) = \frac{|3T|^2}{|4K + T|^2} \sin^4 \theta. \quad (\text{A4})$$

The quantities  $K$  and  $T$  used in equations (A3) and (A4) are given by

$$K = \frac{\epsilon + 2}{\epsilon - 1}, \quad (\text{A5})$$

$$T = \begin{cases} \frac{3}{e^2} \left[ 1 - (1 - e^2)^{1/2} \frac{\sin^{-1} e}{e} \right] - 1 & \text{(oblate),} \\ \frac{3(1 - e^2)}{2e^2} \left[ \frac{1}{e} \ln \left( \frac{1 + e}{1 - e} \right) - 2 \right] - 1 & \text{(prolate).} \end{cases} \quad (\text{A6})$$

## APPENDIX B

### EVALUATION OF TOTAL PARTICLE MASS AND MASS-LOSS RATE

The total mass and radar cross section of a population of particles with size distribution  $n(a)$  and mass density  $\rho$  are given by

$$M = \frac{4}{3} \pi \rho \int_{a_0}^{a_m} n(a) a^3 da, \quad (\text{B1})$$

$$\sigma = \pi \int_{a_0}^{a_m} n(a) Q_b(a) a^2 da, \quad (\text{B2})$$

where  $Q_b$  is the backscatter efficiency and  $a_0$  and  $a_m$  are the minimum and maximum particle sizes in the distribution. In the Rayleigh approximation ( $a \ll \lambda$ ) the backscatter efficiency for a particle of dielectric constant  $\epsilon$  is given by

$$Q_b(a) = C_Q a^4, \quad (\text{B3})$$

where

$$C_Q = 4 \left( \frac{2\pi}{\lambda} \right)^4 \left| \frac{\epsilon - 1}{\epsilon + 2} \right|^2.$$

Assuming  $n(a) \propto a^{-\alpha}$ , then from equations (B1)–(B3) we have ( $\alpha \neq 4$ )

$$\begin{aligned} M &= \frac{4}{3} \pi \rho C_Q^{-1} \left( \frac{7 - \alpha}{4 - \alpha} \right) \left[ \frac{a_m^{4-\alpha} - a_0^{4-\alpha}}{a_m^{7-\alpha} - a_0^{7-\alpha}} \right] \\ &\cong \frac{1}{3} \pi \rho \left( \frac{\lambda}{2\pi} \right)^4 \left| \frac{\epsilon + 2}{\epsilon - 1} \right|^2 \left( \frac{7 - \alpha}{4 - \alpha} \right) \left[ 1 - \left( \frac{a_0}{a_m} \right)^{4-\alpha} \right] a_m^{-3}. \end{aligned} \quad (\text{B4})$$

The mass-loss rate  $\dot{M}$  and radar cross section  $\sigma$  for the case of a particle production distribution  $\dot{n}(a)$  are given by

$$\dot{M} = \frac{4}{3} \pi \rho \int_{a_0}^{a_m} \dot{n}(a) a^3 da, \quad (\text{B5})$$

$$\sigma = \pi \int_{a_0}^{a_m} \dot{n}(a) \tau(a) Q_b(a) a^2 da, \quad (\text{B6})$$

where  $\tau(a)$  is the mean lifetime within the telescope beam of a particle of radius  $a$ . If we ignore the eroding effect of particle sublimation, then  $\tau$  can be taken as the mean particle transit time across the beam. If  $b$  is the half-width of the cylinder defined by the telescope beam at the comet and  $V$  is the particle ejection velocity, we have

$$\tau(a) = \frac{\pi b}{2V(a)}. \quad (\text{B7})$$

If for  $V$  we use the terminal velocity  $V_t$  (from § Ve), then from equations (8)–(10) and equation (B7) we have

$$\tau(a) = (\pi b/2) C_v^{-1} a^{1/2} (1 - a/a_m)^{-1/2}, \quad (\text{B8})$$

where

$$\begin{aligned} C_v &= [(3/2) V_g \dot{\mu} R \rho^{-1}]^{1/2} \\ &= [(8/3) \pi \rho_n G]^{1/2} R a_m^{1/2}. \end{aligned}$$

If we assume that  $\dot{n}(a) \propto a^{-\alpha}$ , then from equations (B5)–(B8) we have

$$\dot{M} = \frac{8}{3} \sigma \rho R \left[ \left( \frac{8\pi}{3} \right) \rho_n G \right]^{1/2} a_m^{9/2-\alpha} \left[ 1 - \left( \frac{a_0}{a_m} \right)^{4-\alpha} \right] \left[ \pi b(4-\alpha) \int_{a_0}^{a_m} \frac{a^{5/2-\alpha} Q_b(a)}{(1-a/a_m)^{1/2}} da \right]^{-1}. \quad (\text{B9})$$

For the general case we must evaluate the integral in equation (B9) numerically. For the Rayleigh regime ( $a < \lambda/2\pi$ ) we have  $Q_b = C_Q a^4$ , in which case the integral equals  $C_Q B(1/2, 15/2 - \alpha) a_m^{15/2-\alpha}$ , where  $B$  is the beta function. Substituting in equation (B9) then gives the Rayleigh approximation for  $\dot{M}$ ,

$$\dot{M} \cong \frac{(8/3) \sigma \rho R [(8\pi/3) \rho_n G]^{1/2} a_m^{-3} [1 - (a_0/a_m)^{4-\alpha}]}{\pi b(4-\alpha) C_Q B(1/2, 15/2 - \alpha)}. \quad (\text{B10})$$

## APPENDIX C

### EVALUATION OF DOPPLER OFFSETS

For any given ejected particle the Doppler frequency offset relative to the nucleus is given by

$$f = -\frac{2\nu}{c} \left( \frac{\mathbf{v}_{pe} \cdot \mathbf{r}_{pe}}{r_{pe}} - \frac{\mathbf{v}_{ce} \cdot \mathbf{r}_{ce}}{r_{ce}} \right), \quad (\text{C1})$$

where  $\nu$  is the frequency of the radar,  $c$  is the speed of light, and the subscripts “pe” and “ce” denote the velocity and position vectors of the particle relative to the Earth and the comet nucleus relative to the Earth, respectively. We can write  $\mathbf{v}_{pe} \cdot \mathbf{r}_{pe} = (\mathbf{v}_{pc} + \mathbf{v}_{ce}) \cdot (\mathbf{r}_{pc} + \mathbf{r}_{ce})$ , where the subscript “pc” denotes the particle velocity or position relative to the comet nucleus. Then using the approximation  $r_{pe}^{-1} \cong r_{ce}^{-1} (1 - \hat{\mathbf{r}}_{ce} \cdot \mathbf{r}_{pc}/r_{ce})$ , where the caret denotes the unit vector, and dropping second-order terms containing  $r_{pe}^2$ , we have the result

$$\frac{\mathbf{v}_{pe} \cdot \mathbf{r}_{pe}}{r_{pe}} \cong r_{ce}^{-1} [\mathbf{v}_{ce} \cdot \mathbf{r}_{pc} + \mathbf{v}_{pc} \cdot \mathbf{r}_{ce} + \mathbf{v}_{ce} \cdot \mathbf{r}_{ce} - (\mathbf{v}_{ce} \cdot \mathbf{r}_{ce}) \left( \frac{\hat{\mathbf{r}}_{ce} \cdot \mathbf{r}_{pc}}{r_{ce}} \right)]. \quad (\text{C2})$$

Then from equations (C1) and (C2) we have

$$f \cong (-2\nu/c) \{ \mathbf{v}_{pc} \cdot \hat{\mathbf{r}}_{ce} + r_{ce}^{-1} [\mathbf{v}_{ce} - (\mathbf{v}_{ce} \cdot \hat{\mathbf{r}}_{ce}) \hat{\mathbf{r}}_{ce}] \cdot \mathbf{r}_{pc} \}. \quad (\text{C3})$$

The first term inside the braces in equation (C3) is the component of Doppler offset from particle motion relative to the nucleus (“velocity component”). The second term is the Doppler component from the geometrical projection of the particle’s spatial separation  $\mathbf{r}_{pc}$  (“spatial component”).

If one ignores radiation pressure and solar tidal forces (see below), then the particles ejected by the simple gas-drag mechanism (§ Ve) are free particles in a frame moving with the comet. Thus we have  $\mathbf{r}_{pc} = \mathbf{v}_{pc}(t_0 - t)$ , where  $t_0$  is the time at which the observations were made and  $t$  is the time at which a given particle was ejected. Then, letting  $\mathbf{v}_{pc} = \hat{\mathbf{v}}_{pc} V_t$  and using equations (8)–(10), we have

$$\begin{aligned} f(a; t, \hat{\mathbf{e}}) &= g(t, \hat{\mathbf{e}}) V_t(a) \\ &= g(t, \hat{\mathbf{e}}) [(8/3) \pi \rho_n G]^{1/2} R a^{-1/2} (a_m - a)^{1/2}, \end{aligned} \quad (\text{C4})$$

where

$$g(t, \hat{\mathbf{e}}) = (-2\nu/c) \{ \hat{\mathbf{v}}_{pc} \cdot \hat{\mathbf{r}}_{ce} + r_{ce}^{-1} [\mathbf{v}_{ce} - (\mathbf{v}_{ce} \cdot \hat{\mathbf{r}}_{ce}) \hat{\mathbf{r}}_{ce}] \cdot \hat{\mathbf{v}}_{pc}(t_0 - t) \}. \quad (\text{C5})$$

Here  $\hat{\mathbf{e}}$  denotes the particle ejection direction at time  $t$ , while all of the vectors on the right-hand side of equation (C5) are evaluated at the observation time  $t_0$ .

Equation (C5) is most easily evaluated in a heliocentric coordinate system whose x-axis is the comet direction at perihelion and whose x-y plane is the comet orbit plane. The azimuth of the comet direction vector  $\hat{\mathbf{r}}_{sc}$  in this frame is the true anomaly  $\theta$  (where  $r_{sc}$  is the Sun-comet distance). We will specify the particle ejection direction  $\hat{\mathbf{e}}$  by the angles  $\xi$  and  $\eta$ , where  $\xi$  is the azimuth angle of the ejection relative to the Sun direction (measured in the comet’s orbital plane) and  $\eta$  is the altitude angle with respect to that plane. The velocity unit vector of this particle at the observation time  $t_0$  is thus given by

$$\hat{\mathbf{v}}_{pc} = \begin{pmatrix} \cos \eta \cos \phi \\ \cos \eta \sin \phi \\ \sin \eta \end{pmatrix}, \quad (\text{C6})$$

where

$$\phi = \theta(t) + \pi + \zeta + \xi. \quad (C7)$$

Here  $\zeta$  denotes the angle by which the comet velocity vector rotates during the time period  $t_0 - t$ .

A full treatment of the particle motion should include both radiation pressure and the tidal force exerted by solar gravity over the extended particle cloud. We have not included the radiation pressure force, since it greatly complicates the particle motion equations without having a significant effect on the IAA model skirt spectrum. The radiation pressure force for a particle of radius  $a$  is equal to  $Q_{pr} E_{\odot} a^2 / (4cr_{sc}^2)$ , where  $Q_{pr}$  is an efficiency factor ( $\cong 1$ ),  $E_{\odot}$  is the solar output ( $3.93 \times 10^{26}$  W) and  $c$  is the speed of light (e.g., Finson and Probst 1968). At  $r_{sc} = 1$  AU this corresponds to an acceleration of  $0.35 \times 10^{-9} \rho^{-1} a^{-1}$  ( $\text{km s}^{-2}$ ), where  $a$  is in centimeters and  $\rho$  is in grams per cubic centimeter, or a particle displacement  $\Delta r$  (km) after a time  $t$  (days) given by  $\Delta r = 1.3t^2/(\rho a)$ . If we let  $t = b/V_t$  (the minimum time for a particle to move out of the Arecibo beam), then one gets  $\Delta r/b = 1.4 \times 10^{-2} \rho^{-1} (a_m - a)^{-1}$ . Thus, if we take  $\Delta r/b$  as a crude measure of the relative importance of radiation pressure to particle motion, we see that the effect of this force on particle displacement amounts to a few percent at most. Unlike the radiation pressure force, the solar tidal force can be approximately corrected for without significantly complicating the equations of motion. This correction has been made by making the substitution  $\hat{v}_{pc} \rightarrow \hat{v}_{pc} + \mathbf{A}$  in the velocity term in equation (C5) and  $\hat{v}_{pc}(t_0 - t) \rightarrow \hat{v}_{pc}(t_0 - t) + \mathbf{B}$  in the spatial term in equation (C5). The correction terms are the vectors given by

$$\mathbf{A} = 2GM_{\odot} \int_t^{t_0} r_{sc}^{-3} \hat{r}_{sc} (\hat{r}_{sc} \cdot \hat{r}_{pc}) (t' - t) dt', \quad (C8)$$

$$\mathbf{B} = 2GM_{\odot} \int_t^{t_0} r_{sc}^{-3} \hat{r}_{sc} (\hat{r}_{sc} \cdot \hat{r}_{pc}) (t' - t)^2 dt', \quad (C9)$$

where  $M_{\odot}$  is the solar mass and where for  $\hat{r}_{pc}$  we use the zeroth-order (uncorrected) value.

The quantities  $\theta$ ,  $r_{sc}$ , and  $\zeta$  were determined from the standard parabolic orbit equations (e.g., Marsden 1983; Taff 1985),

$$\theta = 2 \tan^{-1} z, \quad r_{sc} = q(1 + z^2),$$

where  $q = r_{sc}(T)$  at perihelion time  $T$  and  $z(t')$  is the solution to

$$\frac{1}{3} z^3 + z = \left( \frac{GM_{\odot}}{2q^3} \right)^{1/2} (t' - T).$$

The quantities  $r_{ce}$ ,  $v_{ce}$  were obtained in geocentric equatorial coordinates from the observing ephemeris. These were then transformed to heliocentric comet coordinates by multiplying by the rotation matrix  $\mathbf{M}(\omega, i, \Omega, \epsilon)$  given by Marsden and Roemer (1982). The comet orbit parameters  $\omega$ ,  $i$ ,  $\Omega$ ,  $q$ , and  $T$  were obtained from *IAU Circular 3797* (Marsden 1983).

#### REFERENCES

- Allan, L. E., and McCormick, G. C. 1978, *IEEE Trans.*, **AP-26**, 579.  
 Altenhoff, W. J., Batrla, W., Huchtmeier, W. K., Schmidt, J., Stumpff, P., and Walmsley, M. 1983, *Astr. Ap.*, **125**, L19.  
 Brockelman, R. A., and Hagfors, T. 1966, *IEEE Trans.*, **AP-14**, 621.  
 Brown, R. H., Cruikshank, D. B., and Griep, D. 1985, *Icarus*, **62**, 273.  
 Campbell, D. B., Harmon, J. K., Hine, A. A., Shapiro, I. I., Marsden, B. G., and Pettengill, G. H. 1983, *Bull. AAS*, **15**, 800.  
 Campbell, D. B., Harmon, J. K., and Shapiro, I. I. 1989, *Ap. J.*, **338**, 1094.  
 Campbell, M. J., and Ulrichs, J. 1969, *J. Geophys. Res.*, **74**, 5867.  
 Cuzzi, J. N., and Pollack, J. B. 1978, *Icarus*, **33**, 233.  
 Delsemme, A. H., and Miller, D. C. 1971, *Planet. Space Sci.*, **19**, 1229.  
 de Pater, I., Wade, C. M., Houppis, H. L. F., and Palmer, P. 1985, *Icarus*, **62**, 349.  
 Evans, J. V. 1969, *Ann. Rev. Astr. Ap.*, **7**, 201.  
 Feierberg, M. A., Witteborn, F. C., Johnson, J. R., and Campins, H. 1984, *Icarus*, **60**, 449.  
 Feldman, P. D., A'Hearn, M. F., and Millis, R. L. 1984, *Ap. J.*, **282**, 799.  
 Finson, M. L., and Probst, R. F. 1968, *Ap. J.*, **154**, 327.  
 Gambosi, T. I., Nagy, A. F., and Cravens, T. E. 1986, *Rev. Geophys.*, **24**, 667.  
 Gary, G. A., and O'Dell, C. R. 1974, *Icarus*, **23**, 519.  
 Goldstein, R. M., Jurgens, R. F., and Sekanina, Z. 1984, *A.J.*, **89**, 1745.  
 Hanner, M. S. 1981, *Icarus*, **47**, 342.  
 Hanner, M. S., Aitken, D. K., Knacke, R., McCorckle, S., Roche, P. F., and Tokunaga, A. T. 1985, *Icarus*, **62**, 97.  
 Kamoun, P. G. 1983, Ph.D. thesis, Massachusetts Institute of Technology.  
 Kamoun, P. G., Campbell, D. B., Ostro, S. J., Pettengill, G. H., and Shapiro, I. I. 1982, *Science*, **216**, 293.  
 Kamoun, P. G., Pettengill, G. H., and Shapiro, I. I. 1982, in *Comets*, ed. L. L. Wilkening (Tucson: University of Arizona Press), p. 228.  
 Lutz, B. L., and Wagner, R. M. 1986, *Ap. J.*, **308**, 993.  
 Marsden, B. G. 1983, *IAU Circ.*, No. 3797.  
 Marsden, B. G., and Roemer, E. 1982, in *Comets*, ed. L. L. Wilkening (Tucson: University of Arizona Press), p. 707.  
 Mon, J. P. 1982, *Radio Sci.*, **17**, 953.  
 Oliverson, R. J., Hollis, J. M., and Brown, L. W. 1985, *Icarus*, **63**, 339.  
 Ostro, S. J. 1985, *Pub. A.S.P.*, **97**, 877.  
 Ostro, S. J., Campbell, D. B., and Shapiro, I. I. 1985, *Science*, **229**, 442.  
 Sekanina, Z. 1974, *Icarus*, **23**, 502.  
 ———. 1981, *A.J.*, **86**, 1741.  
 Shapiro, I. I., Marsden, B. G., Whipple, F. L., Campbell, D. B., Harmon, J. K., and Hine, A. A. 1983, *Bull. AAS*, **15**, 800.  
 Storrs, A. D., Tokunaga, A. T., Christian, C. A., and Heasley, J. N. 1986, *Icarus*, **66**, 143.  
 Taff, L. G. 1985, *Celestial Mechanics* (New York: Wiley).  
 Ulaby, F. T., Moore, R. K. and Fung, A. K. 1981, *Microwave Remote Sensing* (Reading, MA: Addison-Wesley).  
 van de Hulst, H. C. 1957, *Light Scattering by Small Particles* (New York: Wiley).  
 Walker, R. G., Aumann, H. H., Davies, J., Green, S., de Jong, T., Houck, J. R., and Soifer, B. T. 1984, *Ap. J.*, **278**, L11.  
 Wallis, M. K. 1982, in *Comets*, ed. L. L. Wilkening (Tucson: University of Arizona Press), p. 357.  
 Walmsley, C. M. 1985, *Astr. Ap.*, **142**, 437.  
 Warner, C. 1978, Department of Environmental Science Rept. (Charlottesville: University of Virginia).  
 Whipple, F. L. 1951, *Ap. J.*, **113**, 464.

D. B. CAMPBELL: Department of Astronomy, Cornell University, Ithaca NY 14853

J. K. HARMON and A. A. HINE: Arecibo Observatory, P.O. Box 995, Arecibo, PR 00613

B. G. MARSDEN and I. I. SHAPIRO: Harvard-Smithsonian Center for Astrophysics, 60 Garden Street, Cambridge, MA 02138